Angular momentum dependent orbital-free density functional theory: Formulation and implementation

Youqi Ke, Florian Libisch, Junchao Xia, and Emily A. Carter,*

Department of Mechanical and Aerospace Engineering, Program in Applied and Computational Mathematics, and Andlinger Center for Energy and the Environment, Princeton University, Princeton, New Jersey 08544-5263, USA

(Received 3 August 2013; revised manuscript received 30 December 2013; published 10 April 2014)

Orbital-free density functional theory (OFDFT) directly solves for the ground-state electron density. It scales linearly with respect to system size, providing a promising tool for large-scale material simulations. Removal of the orbitals requires use of approximate noninteracting kinetic energy density functionals. If replacing ionic cores with pseudopotentials, removal of the orbitals also requires these pseudopotentials to be local. These are two severe challenges to the capabilities of conventional OFDFT. While main group elements are often well described within conventional OFDFT, transition metals remain intractable due to their localized *d* electrons. To advance the accuracy and general applicability of OFDFT, we have recently reported a general angular momentum dependent formulation as a next-generation OFDFT. In this formalism, we incorporate the angular momenta of electrons by devising a hybrid scheme based on a muffin tin geometry: inside spheres centered at the ionic cores, the electron density is expanded in a set of atom-centered basis functions combined with an onsite density matrix. The explicit treatment of the angular momenta of electrons provides an important basis for accurately describing the important ionic core region, which is not possible in conventional OFDFT. In addition to the conventional OFDFT total energy functional, we introduce a nonlocal energy term containing a set of angular momentum dependent energies to correct the errors due to the approximate kinetic energy density functional and local pseudopotentials. Our approach greatly increases the accuracy of OFDFT while largely preserving its numerical simplicity. Here, we provide details of the theoretical formulation and practical implementation, including the hybrid scheme, the derivation of the nonlocal energy term, the choice of basis functions, the direct minimization of the total energy, the procedure to determine the angular momentum dependent energies, the force formula with Pulay correction, and the solution to emerging numerical instability. To test the angular momentum dependent OFDFT formalism and its numerical implementations, we calculate a diverse set of properties of the transition metal Ti and compare with different levels of DFT approximation. The results suggest that angular momentum dependent OFDFT ultimately will extend the reliable reach of OFDFT to the rest of the periodic table.

DOI: 10.1103/PhysRevB.89.155112 PACS number(s): 71.15.Mb, 71.20.Be

I. INTRODUCTION

Based on the firm theoretical footing of the Hohenberg-Kohn theorems [1], density functional theory (DFT) has gained vast popularity as an extremely powerful tool for the first-principles simulation of electronic and structural properties of materials. The great success of DFT is attributed to the Kohn-Sham (KS) decomposition in which the intractable many-electron problem is reduced to a calculable problem of noninteracting electrons moving in an effective potential [2]. Thus far, theorists have developed two ways to implement DFT: KS orbital-based DFT [2] and orbital-free (OF) DFT [3], distinguished by the different treatments of the noninteracting kinetic energy (KE). KSDFT has been established as the workhorse for first-principles simulations due to its good compromise between accuracy and computational efficiency (as compared to more expensive correlated wave function methods) [4]. However, the required orthogonalization of the KS orbitals in standard KSDFT implementations makes the computational cost scale cubically with respect to system size, making a sample with more than a thousand atoms prohibitively costly to simulate. Several different linear scaling KSDFT algorithms have been devised (for reviews, see Refs. [5,6]), albeit with large prefactors. Notably, linear scaling KSDFT methods depend on approximations requiring highly localized orbitals, and their applicability is therefore limited to systems with band gaps, which excludes metallic systems. Consequently, a wide range of important applications, such as first-principles simulations of large-scale nanoelectronics [7], nanomechanics [8], or amorphous materials [9], requiring the ability to explicitly model systems with thousands of atoms (or even more), are challenging or not feasible using modern KSDFT methods. In contrast to KSDFT, OFDFT [3] features great advantages in its numerical simplicity and quasilinear scaling with system size for all types of materials. There are numerous examples of large-scale OFDFT-based simulations that highlight its numerical advantages for cases in which adequate approximate functionals are available [10–19].

OFDFT employs approximate noninteracting KE density functionals (KEDFs), making OFDFT less accurate than KSDFT for almost all materials. Except for limiting cases, such as the local Thomas-Fermi (TF) KEDF [20] for the uniform electron gas and the semilocal von Weizsäcker (vW) KEDF [21] for single orbital systems, the exact form of the KEDF remains unknown. Recently, theorists have made considerable efforts to advance KEDFs, including two-point KEDFs based on linear response theory [22–26], three-point KEDFs involving higher-order response [23,27,28], and single-point KEDFs in different forms of generalized gradient approximations [29–32]. However, we are still far from a generally applicable KEDF.

*eac@princeton.edu

Because conventional OFDFT typically is implemented in the context of plane-wave techniques (such as the fast Fourier transform) and available KEDFs are only suitable for systems featuring comparatively smooth electron densities, pseudopotentials are required to represent the interaction between the valence electrons and the ionic cores. However, conventional OFDFT utilizes local pseudopotentials (LPSs). To obtain optimal LPSs, several techniques have been proposed [14,33–38]. Unfortunately, even elaborate LPS procedures do not produce the high accuracy of nonlocal pseudopotentials (NLPSs) that are widely used in KSDFT.

The applicability of conventional OFDFT is thus largely constrained by the limited accuracy of available KEDFs and LPSs. In particular, one of the most challenging issues for OFDFT is the description of transition metals, which are characterized by highly localized d electrons, for which no KEDF or LPS exists. Exceptions are the coinage metals, such as Ag, which is a special case because of their full d shells [39].

These difficulties occur because conventional OFDFT makes exclusive use of the total electron density as the sole working variable: electrons with different angular momenta cannot be distinguished. It is therefore impossible to include the critically important nonlocal physics in the exact KE and the ion-electron interaction, especially in the core region. In particular, the KE potential and the pseudopotentials in OFDFT must be local quantities. By contrast, angular momentum dependent (AMD) NLPSs and the exact KE operator containing an AMD centrifugal potential are responsible for the high accuracy and excellent transferability of the Kohn-Sham ansatz. Furthermore, because of the nonlinear dependence of T_s^{KEDF} on ρ, using the total electron density in conventional OFDFT can induce unphysical interactions between electrons of different angular momenta. In contrast, the exact KE depends linearly on the occupation of each angular momentum channel. These unphysical interactions in the KEDF can result in errors in the KE potential which, in turn, influence the electron density distribution. In addition, the modern two-point KEDFs [22–24], which are the most accurate KEDFs to date, reproduce the Lindhard linear response function in the limit of a uniform electron gas subject to a small perturbation [22–24]. They are thus only accurate for nearly free-electron-like systems, i.e., main group metals and their alloys. The application of conventional OFDFT to localized electrons, e.g., in transition metals, can result in large errors in the electron density, its response to external fields, and ultimately in system properties [40].

To correct these deficiencies, we have recently developed angular momentum dependent OFDFT (AMD-OFDFT) [41], a new generation of OFDFT to advance its accuracy and general applicability. The AMD-OFDFT formalism uses a general hybrid scheme based on a muffin tin (MT) geometry: the electron density inside MT spheres is expressed by a set of KSDFT-derived, atom-centered basis functions combined with an onsite density matrix, while conventional OFDFT describes the interstitial region where the electron density is smoother and hence more amenable to accurate description by existing KEDFs. The explicit treatment of electron angular momenta within the atom-centered spheres provides the basis for accurately describing the important ionic core region. In addition to the total energy functionals of conventional OFDFT, we introduce a crucial nonlocal energy term that includes a set of AMD energies to effectively correct errors due to the approximate KEDFs and LPSs in the important core region, resulting in improved electronic structure and system properties. As we have shown [41], AMD-OFDFT substantially improves various properties of the transition metal titanium over conventional OFDFT, and features good transferability of the AMD energies.

In this paper, we present the entire theoretical formulation and all practical implementation details of the general AMD-OFDFT. In Sec. II, we introduce a hybrid scheme based on a MT geometry, a general OFDFT total energy functional with angular momentum dependence, and a nonlocal energy term and its associated AMD energy parameters which corrects the errors due to the use of approximate KEDFs and LPSs. Section III presents the derivation of the atom-centered basis functions in the MT spheres based on KSDFT-NLPS calculations of target systems. We then discuss the direct minimization of AMD-OFDFT total energy functional with the necessary constraints applied in Sec. IV. Section V describes the modified KEDF model with a weighting function to reduce nonlinear errors of the KEDF within the MT geometry. Section VI details how to determine the AMD onsite energies for the MT spheres. We derive a force formula with a Pulay correction (arising from the atom-centered functions) in Sec. VII. In Sec. VIII, we introduce a double-sphere technique and a down-sampling approach for solving the numerical instability induced by representing the MT spheres on a nonconforming three-dimensional (3D) uniform grid. We present computational details and discuss our results in Sec. IX. Finally, we provide a summary in Sec. X, and additional technical details in Appendices A, B, and C.

II. AMD-OFDFT TOTAL ENERGY

Several all-electron KSDFT methods, such as the linearized augmented plane-wave (LAPW) [42] and the linearized muffin tin orbital (LMTO) [43] methods, are based on a MT geometry. In such a geometry, the system is partitioned into atom-centered MT spheres and an interstitial region (see Fig. 1). Here, we use a MT geometry to define a general OFDFT

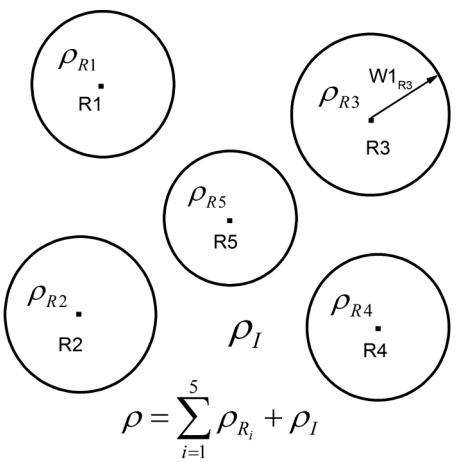

FIG. 1. The muffin tin geometry partitions space into spheres centered on nuclei and an interstitial region.

total energy functional with explicit angular momentum dependence.

Within the MT geometry, we rewrite the total electron density as [41]

$$\rho(\vec{r}) = \sum_R \rho_R(\vec{r}_R) + \rho_I(\vec{r}), \tag{1}$$

where $\rho_R(\vec{r}_R)$ is the electron density inside the MT sphere with a radius $W1_R$ centered on site $\vec{R}$, $\rho_I(\vec{r})$ is the interstitial electron density, and $\vec{r}_R = \vec{r} - \vec{R}$. To explicitly include angular momentum dependence, we introduce a set of fixed atom-centered basis functions $\psi_{R,lm} = \phi_{R,l}(r_R)Y_{lm}(\Omega)$, where Y_{lm} are the spherical harmonics. We can now express ρ_R as

$$\rho_R(\vec{r}_R) = \sum_{lm,l'm'} N_{R,lm,l'm'}\psi^*_{R,lm}(\vec{r}_R)\psi_{R,l'm'}(\vec{r}_R). \tag{2}$$

We omit the spin index throughout this paper for simplicity. N_R denotes the onsite density matrix which contains information on the angular momenta of electrons. For atoms with significant hybridization between different channels, the off-diagonal elements of $N_{R,lm,lm}$ are important for improving nonsphericity of electron density inside the MT sphere. Using Eqs. (1) and (2), the OFDFT total energy functional can be rewritten as

$$E^{\mathrm{OF}}[\rho] = E^{\mathrm{OF}}[\{N_R\},\rho_I], \tag{3}$$

where the onsite density matrix $\{N_R\}$ and the interstitial electron density ρ_I become the basic independent variables. Up to now, no physical approximation has been made to the OF total energy functional. Errors in the electron density inside the spheres due to use of a finite basis set can be minimized by an appropriate choice of the $\psi_{R,lm}$; our strategy for deriving basis functions from NLPS-based KSDFT calculations is presented in Sec. III. We typically use a comparatively small number of basis functions. Compared to conventional OFDFT, using such a finite number of basis functions strongly restricts the shape of the electron density inside the MT spheres. However, this restriction results in a more accurate electron density than in conventional OFDFT: the nonlocal effect of the KE operator and the NLPS on the shape of the electron density are included by using basis sets derived from KSDFT. Additionally, the total energy functional in Eq. (3) incorporates angular momentum dependence by using N_R for the MT sphere region where the AMD physics is most important. Consequently, our hybrid scheme provides the physical flexibility to include AMD contributions not feasible in conventional implementations of OFDFT.

The explicit form of $E^{\mathrm{OF}}[\{N_R\},\rho_I]$ can be written as [41]

$$\begin{aligned} E^{\mathrm{OF}}[\{N_R\},\rho_I] = {} & T_s^{\mathrm{KEDF}}[\rho] + E_{\mathrm{XC}}[\rho] + E_{\mathrm{H}}[\rho] \\ & + E_{\mathrm{i\text{-}e}}^{\mathrm{LPS}}[\rho] + E^{\mathrm{NL}}[\{N_R\},\rho_I], \end{aligned} \tag{4}$$

where the energies T_s^{KEDF}, E_{H}, E_{XC}, and $E_{\mathrm{i\text{-}e}}^{\mathrm{LPS}}$ are the noninteracting KE, Hartree energy, exchange-correlation energy, and LPS energy, respectively. The first four terms comprise the conventional OFDFT total energy functional. E^{NL} describes nonlocal contributions beyond conventional OFDFT. It corrects the errors due to the approximate T_s^{KEDF} and LPSs. Determining a physically sensible E^{NL} is critical for correct electronic structure and material properties, forming the crux of our AMD-OFDFT formalism [41].

Ideally, E^{NL} should contain all the differences between the KSDFT and conventional OFDFT total energy functionals, namely,

$$E^{\mathrm{NL}} = E_{\mathrm{i\text{-}e}}^{\mathrm{NLPS}} + T_s - T_s^{\mathrm{KEDF}}, \tag{5}$$

where $E_{\mathrm{i\text{-}e}}^{\mathrm{NLPS}}$ is only the nonlocal part of the pseudopotential energy and $T_s - T_s^{\mathrm{KEDF}}$ is the KE error. Note that the nonlocal part of the pseudopotential is not uniquely defined since it depends on the choice of the local pseudopotential. Consequently, $E_{\mathrm{i\text{-}e}}^{\mathrm{NLPS}}$ depends on $E_{\mathrm{i\text{-}e}}^{\mathrm{LPS}}$; together they define a unique total nonlocal pseudopotential energy. The exact computation of E^{NL} requires the exact KEDF which is unknown. We follow here our derivation for E^{NL} in Ref. [41], which we briefly repeat for completeness. We choose the MT sphere radius for each element large enough so that the nonlocal part of the pseudopotential becomes zero in the interstitial region. The minimal MT sphere radius is thus the cutoff radius r_{cutoff} of the NLPS used in solving for the basis functions (see Sec. III).

As amply demonstrated in many applications, modern KEDFs [22–24] based on the Lindhard response function exhibit accuracy comparable to KSDFT for main group metals. Therefore, these KEDFs should be accurate enough to describe the slowly varying electron density found in the interstitial region. We thus neglect $T_s - T_s^{\mathrm{KEDF}}$ there, using conventional OFDFT to treat the interstitial region. Unfortunately, two different representations of the KE result in a discontinuous KE potential at the sphere boundary, causing unphysical electron occupations. We thus enforce continuity by formally introducing a smooth scaling function $s_R(r)$ [$s_R(r) = 0$ for $r \geqslant W1_R$ and $0 \leqslant s_R(r) \leqslant 1$ for $r < W1_R$] in the evaluation of the $T_s - T_s^{\mathrm{KEDF}}$ inside the spheres, providing a rigorous hybrid KEDF model (see details in the Supplemental Material of Ref. [41]). Then E^{NL} becomes

$$\begin{aligned} E^{\mathrm{NL}} &= E_{\mathrm{i\text{-}e}}^{\mathrm{NLPS}} + \sum_R \int_{\mathrm{MT}} s_R(r_R)\left[\tau_s(\vec{r}_R) - \tau_s^{\mathrm{KEDF}}(\vec{r}_R)\right]d\vec{r}_R \\ &= E_{\mathrm{i\text{-}e}}^{\mathrm{NLPS}} + [\tilde{T}_s]_{\mathrm{MT}} - \left[\tilde{T}_s^{\mathrm{KEDF}}\right]_{\mathrm{MT}}, \end{aligned} \tag{6}$$

where $[\tilde{T}_s]_{\mathrm{MT}}$ and $[\tilde{T}_s^{\mathrm{KEDF}}]_{\mathrm{MT}}$ are the exact noninteracting KE and the KEDF scaled by s_R inside the MT spheres. Equation (6) presents a physically reasonable expression for E^{NL}, providing an important basis for further development of AMD-OFDFT. However, determining the optimal function values of $s_R(r_R)$ on a large number of radial grid points is too costly for practical use. Instead, we investigate the functional dependence of each term in Eq. (6) on the occupations N_R to determine a more practical expression containing the same physics.

We first consider $E_{\mathrm{i\text{-}e}}^{\mathrm{NLPS}}$ and $[\tilde{T}_s]_{\mathrm{MT}}$ in Eq. (6). They depend linearly on the total occupation number of each l channel. In particular,

$$\begin{aligned} E_{\mathrm{i\text{-}e}}^{\mathrm{NLPS}}[N_R] &= \sum_{R,lm} N_R^{lm}\langle\psi_{R,lm}|\delta V_{\mathrm{i\text{-}e}}^l|\psi_{R,lm}\rangle_{\mathrm{MT}} \\ &= \sum_{R,l} N_{R,l}^{\mathrm{total}} E_R^{l,\mathrm{NLPS}} \end{aligned} \tag{7}$$

and

$$[\tilde{T}_s]_{\mathrm{MT}} = -\frac{1}{2}\sum_{R,lm} N_R^{lm}\langle\psi_{R,lm}|s_R\nabla^2|\psi_{R,lm}\rangle_{\mathrm{MT}} = \sum_{R,l} N_{R,l}^{\mathrm{total}} E_R^{l,T_s}, \tag{8}$$

where $\delta V_{\mathrm{i\text{-}e}}^l$ is the nonlocal part of the pseudopotential, $N_{R,l}^{\mathrm{total}} = \sum_{m=-l}^{l} N_R^{lm}$, and we have introduced the shorthand notation $N_R^{lm} = N_{R,lm,lm}$. $E_R^{l,\mathrm{NLPS}}$ and E_R^{l,T_s} are constants that depend on the shape of the basis functions of each l channel. Consequently, a linear term in E^{NL} can easily accommodate the AMD effects of $E_{\mathrm{i\text{-}e}}^{\mathrm{NLPS}}$ and $[\tilde{T}_s]_{\mathrm{MT}}$.

Next, we derive the linear and dominant nonlinear terms in the employed KEDF to allow for their correction by E^{NL}. We Taylor expand a general KEDF $[\tilde{T}_s^{\mathrm{KEDF}}]_{\mathrm{MT}}[N_R]$ up to third order around the average occupation number of each l channel $N_{R,l}^0 = N_{R,l}^{\mathrm{total}}/(2l+1)$ to obtain

$$\left[\tilde{T}_s^{\mathrm{KEDF}}\right]_{\mathrm{MT}}[N] = \left[\tilde{T}_s^{\mathrm{KEDF}}\right]_{\mathrm{MT}}\left[\{N_{R,l}^0\}\right] + \sum_{R,lm}\left.\frac{\partial\left[\tilde{T}_s^{\mathrm{KEDF}}\right]_{\mathrm{MT}}}{\partial N_R^{lm}}\right|_{\{N_{R,l}^0\}}\Delta N_R^{lm} + \frac{1}{2}\sum_{R,lm,l'm'}\left.\frac{\partial^2\left[\tilde{T}_s^{\mathrm{KEDF}}\right]_{\mathrm{MT}}}{\partial N_R^{lm}\partial N_R^{l'm'}}\right|_{\{N_{R,l}^0\}}\Delta N_R^{lm}\Delta N_R^{l'm'} + \frac{1}{6}\sum_{R,lm,l'm',l''m''}\left.\frac{\partial^3\left[\tilde{T}_s^{\mathrm{KEDF}}\right]_{\mathrm{MT}}}{\partial N_R^{lm}\partial N_R^{l'm'}\partial N_R^{l''m''}}\right|_{\{N_{R,l}^0\}}\Delta N_R^{lm}\Delta N_R^{l'm'}\Delta N_R^{l''m''} + O\left(\Delta N_R^4\right), \tag{9}$$

where $\Delta N_R^{lm} = N_R^{lm} - N_{R,l}^0$. We neglect the contribution of off-diagonal elements of the density matrix because different l channels hybridize minimally in the core region. Each term in the above Taylor expansion plays a different role. We thus consider individually each term of Eq. (9) in the following.

The zeroth-order term $[\tilde{T}_s^{\mathrm{KEDF}}]_{\mathrm{MT}}[\{N_{R,l}^0\}]$ determines the absolute magnitude of the KE and the total occupation of each l channel inside the spheres. We can expand this term further according to different physical situations. In transition metals, the electron density in the core region is dominated by the total d-channel contribution, i.e., $N_{R,d}^{\mathrm{total}} \gg \{N_{R,s}^{\mathrm{total}}, N_{R,p}^{\mathrm{total}}\}$. Therefore, we make another Taylor expansion of $[\tilde{T}_s^{\mathrm{KEDF}}]_{\mathrm{MT}}[\{N_{R,l}^0\}]$ at $N_{R,s}^0 = N_{R,p}^0 = 0$ because of the small contribution of s/p channels:

$$\left[\tilde{T}_s^{\mathrm{KEDF}}\right]_{\mathrm{MT}}\left[N_{R,l}^0\right] = \left[\tilde{T}_s^{\mathrm{KEDF}}\right]_{\mathrm{MT}}\left[N_{R,l}^0\right]\big|_{N_{R,s/p}^0=0} + \sum_{l'=s,p}\left.\frac{\partial\left[\tilde{T}_s^{\mathrm{KEDF}}\right]_{\mathrm{MT}}\left[N_{R,l}^0\right]}{\partial N_{R,l}^0}\right|_{N_{R,s/p}^0=0} N_{R,l'}^0 + \cdots. \tag{10}$$

We only consider terms up to first order in this paper. It is clear that $[\tilde{T}_s^{\mathrm{KEDF}}]_{\mathrm{MT}}[\{N_{R,l}^0\}]|_{N_{R,s/p}^0=0}$ and $\frac{\partial[T_s^{\mathrm{KEDF}}]_{\mathrm{MT}}[N_{R,l}^0]}{\partial N_{R,l}^0}|_{N_{R,s/p}^0=0}$ only depend on $N_{R,d}^0$ of the localized electrons. As shown in the Supplemental Material of Ref. [41], for modern two-point KEDFs [22–24], we can approximate the zeroth-order term of Eq. (10) as

$$\left[\tilde{T}_s^{\mathrm{KEDF}}\right]_{\mathrm{MT}}\left[N_{R,l}^0\right] \approx V_R^{d,\mathrm{KEDF}}\left(N_{R,d}^{\mathrm{total}}\right)^{\frac{5}{3}} + \sum_{R,l} N_{R,l}^{\mathrm{total}} E_R^{l,\mathrm{KEDF}}, \tag{11}$$

where $E_R^{l,\mathrm{KEDF}}$ and $V_R^{d,\mathrm{KEDF}}$ are constants.

For the first-order term in Eq. (9), the contributions of local and semilocal KEDFs, such as the TF and vW terms in the two-point KEDFs, are zero (see the Supplemental Material of Ref. [41]) because of the spherical electron density distribution when $N_R^{lm} = N_{R,l}^0$ inside the MT sphere. However, for the two-point KEDF, the first derivative of its nonlocal part T_s^{NL}, i.e., $\frac{\partial T_s^{\mathrm{NL}}}{\partial N_R^{lm}}|_{\{N_{R,l}^0\}}$, depends on the quantum number m, contributing a first-order error in Eq. (9). Since contributions of the nonlocal term T_s^{NL} are small in comparison to the TF and vW terms in the two-point KEDFs, we neglect the first-order term in Eq. (9).

We now consider the second- and third-order terms for different KEDFs in Eq. (9). Since the s channel has only a single m value, $N_{R,s} - N_{R,s}^0 = 0$, it does not contribute. We neglect contributions from the p channel since they are small for transition metals. For the remaining d channel, the second- and third-order coefficients can be written as (see the Supplemental Material of Ref. [41])

$$\frac{1}{2}\left.\frac{\partial^2\left[\tilde{T}_s^{\mathrm{KEDF}}\right]_{\mathrm{MT}}}{\partial N_R^{dm}\partial N_R^{dm'}}\right|_{\{N_{R,l}^0\}} = U_R^{\mathrm{KEDF},d} A_{dm,dm'} \tag{12}$$

and

$$\frac{1}{6}\left.\frac{\partial^3\left[\tilde{T}_s^{\mathrm{KEDF}}\right]_{\mathrm{MT}}}{\partial N_R^{lm}\partial N_R^{lm'}\partial N_R^{lm''}}\right|_{\{N_{R,l}^0\}} = K_R^{\mathrm{KEDF},d}\Lambda_{d,m,m',m''}, \tag{13}$$

where $A_{dm,dm'} = 4\pi\int|Y_{dm}Y_{dm'}|^2 d\Omega$ and $\Lambda_{d,m,m',m''} = (4\pi)^2\int|Y_{dm}Y_{dm'}Y_{dm''}|^2 d\Omega$ are constants independent of the atomic species, and are evaluated numerically using a Lebedev quadrature grid [44]. The prefactors $U_R^{\mathrm{KEDF},d}$ and $K_R^{\mathrm{KEDF},d}$, treated as constants in the present method, are determined by a fitting procedure (see Sec. VI). The dependence of $U_R^{\mathrm{KEDF},d}$ and $K_R^{\mathrm{KEDF},d}$ on the occupations N_R could also be considered (see Appendix A).

In summary, by combining Eqs. (6)–(9) and (11)–(13), we obtain a general form for E^{NL} of

$$E^{\mathrm{NL}}[\{N_R\}] = \sum_{R,l} E_R^l N_{R,l}^{\mathrm{total}} - \sum_{R,l} V_R^l\left(N_{R,l}^{\mathrm{total}}\right)^{5/3} - \sum_{R,l,mm'} U_R^l A_{l,mm'}\Delta N_R^{lm}\Delta N_R^{lm'} - \sum_{R,l,mm'm''} K_R^l\Lambda_{l,mm'm''}\Delta N_R^{lm}\Delta N_R^{lm'}\Delta N_R^{lm''}. \tag{14}$$

The above derivation is based on transition metals where the d channel dominates the core region. However, our formulation can be easily generalized to systems with s or p channel dominating the ionic core region, such as in first row elements. We have introduced the onsite AMD energies E_R^l, V_R^l, U_R^l, and K_R^l. We chose V_R^l, U_R^l, and K_R^l nonzero only for l channels featuring localized electrons, such as the d channel in transition metals or the p channel in main group nonmetals. At present, we treat E_R^l, V_R^l, U_R^l, and K_R^l as constants, neglecting their dependence on the occupation numbers. As we show in Sec. IX (see also Ref. [41]), Eq. (14) yields a significant improvement in accuracy for an OFDFT description of transition metals. The AMD energies E_R^l and V_R^l are introduced to correct the relative energies of different l-channel electrons inside the MT spheres, as well as of the electrons in the interstitial region. They are thus crucial for obtaining correct occupations inside the MT spheres. The first (linear) term of Eq. (14) includes the NLPS energy and the correction for the linear errors in the KE inside the MT spheres. The form of $N^{5/3}$ for the V_R^l term corrects the leading nonlinear error in the KEDF, arising from the highly nonlinear TF KEDF term (see Appendix A). The first and second terms in Eq. (14) are important for the absolute magnitude of the total energy of the system. The last two terms in Eq. (14), especially the third term containing U_R^l, are introduced to correct the delocalization error in KEDFs, which arises from unphysical interactions between the different m states of a given l channel. The higher-order terms proportional to U_R^l and K_R^l in Eq. (14) are important for correctly distributing electrons among the $2l+1$ subchannels within one l channel. The third term in our model is mathematically identical to the KSDFT$+U$ formalism, which corrects the self-interaction error in the XC functional due to approximate exchange energy [45]. We benchmark our OFDFT calculations against KS calculations using the same XC functional without a Hubbard U. The improvements we observe are thus related to the correction for the delocalization error in the kinetic energy, not the exchange energy. Our formalism could be trivially extended to include a KSDFT$+U$ like contribution.

Despite the obvious importance of E^{NL} in Eq. (14), directly evaluating the energies E_R^l, V_R^l, U_R^l, and K_R^l is challenging. Instead, we find optimal values for these AMD energies by comparing with a small set of benchmark KSDFT properties, and then test transferability of these parameters against a large number of additional properties.

We have introduced the formulation of AMD-OFDFT by applying a MT-geometry-based hybrid scheme. In the present method, overlapping spheres are not allowed since we do not yet have an effective way to remove errors due to double counting in the overlapping region. As stated above, the lower bound for the MT sphere radius is r_{cutoff} of the NLPS. Since the r_{cutoff} can be rather small and E^{NL} also corrects the KEDF errors inside the spheres, the actual radii of the MT spheres are essentially determined by the magnitude of acceptable errors for a given simulation and as well as the quality of the KEDF employed. If the KEDF is accurate enough to describe a larger interstitial region, the MT sphere radius can be smaller, perhaps as small as the r_{cutoff}.

III. DERIVING BASIS FUNCTIONS FROM BULK OR MOLECULAR KSDFT CALCULATIONS

An accurate description of the important MT sphere region critically depends on the quality of the basis functions, which are fixed throughout the AMD-OFDFT calculations. In this section, we propose a method to derive the atom-centered basis functions $\psi_{R,lm}$ from a NLPS-based KSDFT calculation of a target system. For each element, basis functions are determined by numerical integration of the Schrödinger equation

$$\left[-\frac{\nabla^2}{2}+V(r_R)+\delta V^l_{\text{i-e},R}(r_R)-\epsilon^l_R\right]\psi_{R,lm}=0, \tag{15}$$

where $V(r_R)$ is the spherical effective potential composed of the spherical part of the Hartree potential, the local pseudopotential, and the XC potential, $\delta V^l_{\text{i-e},R}(r_R)$ is the nonlocal part of the ion-electron pseudopotential, and ϵ^l_R is the energy value at which we solve the differential equation for $\psi_{R,lm}$. To solve Eq. (15), we have to know two basic quantities: the spherical potential $V(r_R)$ and the energy ϵ^l_R. The choice of these quantities is critical for the accuracy of our calculation and the transferability of the basis functions. One may obtain approximations for both of these quantities from a single-atom KSDFT calculation. However, this solution does not include the correct chemical environment of the solid and thus can not yield satisfactory accuracy and transferability. Instead, we obtain $V(r_R)$ and ϵ^l_R from KSDFT calculations in a chemical environment similar to the one we are interested in simulating with OFDFT, to minimize errors due to the use of a finite set of $\psi_{R,lm}$. In this way, we properly account for the effect of the chemical environment in solids or molecules in the basis functions.

We expand the bulk (or molecular) $V(\vec{r}_R)$ in terms of spherical harmonics as

$$V(\vec{r}_R)=\sum_{lm}V_{lm}(r_R)Y_{lm}(\hat{\vec{r}}_R). \tag{16}$$

We are only interested in the spherical component of $V(\vec{r}_R)$ for use in Eq. (15). To obtain this component, we first calculate $V(\vec{r}_R)$ including the Hartree, local pseudopotential, and XC potentials on a 3D uniform grid by a self-consistent KSDFT calculation with the same NLPS as Eq. (15). Then we make a fast Fourier transform (FFT) to obtain

$$V(\vec{G})=\mathrm{FFT}[V(\vec{r}_R)]. \tag{17}$$

After calculating the potential in reciprocal space (i.e., on the $\vec{G}$ grid), the spherical $V(r_R)$ on a radial grid is obtained by the integration

$$V(r_R)=\frac{1}{4\pi}\int d\hat{r}_R\int V(\vec{G})e^{i\vec{r}_R\cdot\vec{G}}d\vec{G}, \tag{18}$$

in which we first do an inverse Fourier transform followed by a spherical average to obtain the spherical potential. The above double integration can be reduced to a Bessel transform

$$V(r_R)=\int V(\vec{G})e^{ir_R\cdot G}\frac{\sin(Gr_R)}{Gr_R}d\vec{G}. \tag{19}$$

To solve Eq. (15), we still need to determine the appropriate energy values ϵ^l_R for each l channel. This is achieved by

obtaining the local density of states $n_R^l(E)$ within the MT sphere radius centered on R from the above KSDFT-NLPS calculation, and evaluating ϵ_R^l as the average energy of each angular momentum channel l,

$$\epsilon_R^l = \int_{-\infty}^{E_F} E \frac{n_R^l(E)}{N_R^l} dE, \tag{20}$$

where N_R^l is the total occupation number in channel l,

$$N_R^l = \int_{-\infty}^{E_F} n_R^l(E) dE. \tag{21}$$

All KSDFT calculations are carried out using the ABINIT package [46]. After obtaining ϵ_R^l and $V_R(r_R)$, the Schrödinger equation (15) is solved by integrating from $r_R = 0$ outward to the atomic sphere radius using the fourth-order Runge-Kutta method (no boundary condition is needed since it is not an eigenstate problem) [47]. We find that the basis functions derived in this way exhibit good transferability within similar chemical environments (see Sec. IX). Note that our AMD-OFDFT formalism would in principle allow for multiple radial basis functions $\{\phi_{R,l}^{(1)}, \phi_{R,l}^{(2)}, \ldots\}$ for each l channel to obtain higher accuracy, as usually done, e.g., for Gaussian basis sets in quantum chemistry. However, we only use one radial basis function for each l channel in the applications presented herein.

IV. DIRECT MINIMIZATION OF THE TOTAL ENERGY FUNCTIONAL

Given a set of atom-centered basis functions inside the MT spheres and AMD energies E_R^l, V_R^l, U_R^l, and K_R^l for each atomic sphere, the total energy functional in Eq. (4) can be directly minimized to obtain the ground-state electron density for a fixed ion configuration. To ensure that the total number of electrons is conserved, we perform a constrained minimization of $E^{\mathrm{OF}}[\{N_R\}, \rho_I]$ by applying a Lagrange multiplier μ:

$$L[X] = E[X] - \mu(N_{\mathrm{total}}[X] - N_0). \tag{22}$$

Here, μ defines the chemical potential, the variable $X = \{N_R\}, \rho_I$, and N_0 is the total number of electrons contained in the system. $N_{\mathrm{total}}[X]$ is the electron number functional expressed as

$$N_{\mathrm{total}}[X] = \int_{\mathrm{interstitial}} \rho_I(r) dr + \sum_R \sum_{lm} N_{R,lm,lm} \times \int_{\mathrm{MT},R} \psi_{R,lm}^*(\vec{r}_R) \psi_{R,lm}(\vec{r}_R) dr_R.$$

Only the diagonal part of the onsite density matrix contributes in the above equation because all the off-diagonal elements are eliminated by orthogonality of the different spherical harmonics.

To satisfy the Pauli exclusion principle, we normalize the basis functions inside the MT spheres and then constrain the onsite density matrix to ensure the occupation of each lm channel always lies between zero and one:

$$0 \leqslant N_{R,lm,lm} \leqslant 1. \tag{23}$$

In addition, the same constraint has to be applied to the occupation in each grid cell

$$0 \leqslant \rho_I dV \leqslant 1, \tag{24}$$

where dV is the volume of the unit cell of a uniform grid. To satisfy the above constraints during the minimization process, we rewrite the density matrix N and the interstitial density using the McWeeny purification function [48]

$$N_R = 3M_R^2 - 2M_R^3 \tag{25}$$

and

$$\rho_I dV = \left(3Q_I^2 - 2Q_I^3\right), \tag{26}$$

where M_R and Q_I are, respectively, the auxiliary onsite density matrix and the auxiliary interstitial charge, which directly yield the physical density matrix and interstitial charge. By setting the initial values for the auxiliary quantities M_R and Q_I within the range [0, 1], the constraints in Eqs. (23) and (24) are satisfied automatically during the minimization [48]. Our working variables in Eq. (22) are changed to $Y = M_R, Q_I$, yielding

$$L[X[Y]] = L[Y] = E[Y] - \mu(N_{\mathrm{total}}[Y] - N_0). \tag{27}$$

Direct minimization of $L[Y]$ can be carried out using gradient-based methods, such as conjugate gradient [49] or quasi-Newton methods [50]. The total energy minimum is obtained when

$$\frac{dL}{dY} = \frac{dE}{dY} - \mu \frac{dN_{\mathrm{total}}}{dY} = 0. \tag{28}$$

For technical details of the minimization, see Appendix B.

Finally, we briefly consider the smoothness of the ground-state electron density at the sphere boundary. There are two mechanisms that can drive the electron density to smoothness in the MT geometry: (i) as outlined in Sec. II, the AMD-OFDFT total energy is derived based on a rigorous hybrid KE model. In this hybrid KE model, the KE energy density and the KE potential are continuous at the MT sphere boundary. Since a discontinuous total energy density (or its derivatives) can induce discontinuities in the electron density (or its gradients), the hybrid KE model provides a basis for the continuity of the electron distribution at the minimum of total energy. (ii) Using the vW KEDF (contained in the modern two-point KEDFs [22–24]) further drives the density and its gradient to smoothness. A large gradient in the density gives a large positive vW KE contribution, and thus will increase the total energy. The total energy minimization procedure thus smoothens the electron density by optimizing its gradient.

V. A WEIGHTED KEDF FOR THE ENTIRE SYSTEM WITH REDUCED ERRORS

A sophisticated KEDF model is critical for accurately describing the electron density in the interstitial region, especially for systems containing localized electrons. In addition, it is also very important to have a KEDF model with reduced nonlinear errors inside the MT spheres, so that the form of E^{NL} in Eq. (14) can be more accurate and more easily determined. The KEDFs currently available do not properly treat the rapid density variations that occur in the core region.

In this section, we therefore introduce two general strategies to improve the KEDF model: (i) a weighting function to suppress the (inaccurate) KEDF contributions inside the MT spheres; (ii) pseudized basis functions for the highly localized electron channel dominant in the core region.

Among the linear-response-function-based two-point KEDFs [22–24], the Wang-Govind-Carter (WGC99) KEDF [24] exhibits comparatively high accuracy due to its double-density-dependent response kernel. The WGC99 KEDF can be written as

$$\begin{aligned} T_s^{\mathrm{KEDF}}[\rho] &= T_s^{\mathrm{TF}}[\rho] + T_s^{\mathrm{vW}}[\rho] + T_s^{\mathrm{NL}}[\rho], \\ T_s^{\mathrm{TF}}[\rho] &= C_{\mathrm{TF}} \int \rho^{5/3}(\vec{r}) d\vec{r}, \\ T_s^{\mathrm{vW}}[\rho] &= 1/8 \int [\nabla\rho(\vec{r})]^2/\rho(\vec{r}) d\vec{r}, \\ T_s^{\mathrm{NL}}[\rho] &= \int \rho^{\alpha}(\vec{r}) k[\rho(\vec{r}),\rho(\vec{r}'),\vec{r},\vec{r}']\rho^{\beta}(\vec{r}') d\vec{r} d\vec{r}', \end{aligned} \tag{29}$$

where $T_s^{\mathrm{TF}}[\rho]$ is the Thomas-Fermi KEDF [20], $T_s^{\mathrm{vW}}[\rho]$ is the von Weizäcker KEDF [21], and $T_s^{\mathrm{NL}}[\rho]$ is a nonlocal term introduced to yield the correct linear response of the system. The nonlocal kernel $k[\rho(\vec{r}),\rho(\vec{r}'),\vec{r},\vec{r}']$ is determined by enforcing the Lindhard response at the limit of a uniform electron gas [22–24]. The direct application of this KEDF to inhomogeneous or strongly localized electron densities can result in large quantitative (or even qualitative) errors in electronic structure and material properties compared to KSDFT [40].

To obtain a better description of localized electrons that are tightly bound in the core region, we exploit the hybrid scheme based on the MT geometry. We introduce a weighted KEDF model: we scale available KEDFs using a weighting function $W(\vec{r})$, which equals one inside the interstitial region and smoothly decays to zero inside the MT spheres. $W(\vec{r})$ can be written as

$$W(\vec{r}) = 1 - \sum_R w_R(r_R). \tag{30}$$

We choose the smooth function $w_R(r_R)$ to be

$$w_R(r_R) = \left\{1 - \mathrm{erf}\left[B_R\left(r_R + r_R^w\right)\right]\right\}/2, \tag{31}$$

where erf is the error function, and $0 \leqslant w(r_R) \leqslant 1$. The parameters B_R and r_R^w are chosen by giving function values at the MT sphere boundary $r_R = W1_R$ of $w_R(W1_R) \approx 0$, and at an inner radius $r_{R,1} < W1_R$ of $w_R(r_{R,1}) \lesssim 1$ [see Fig. 2 for $w_R(r_R)$]. Utilizing $W(\vec{r})$, we obtain a weighted KEDF model as follows:

$$\begin{aligned} T_s^{\mathrm{TF}} &= C_{\mathrm{TF}} \int W(\vec{r})\rho^{5/3}(\vec{r}) d\vec{r}, \\ T_s^{\mathrm{vW}} &= 1/8 \int W(\vec{r}) \frac{[\nabla\rho(\vec{r})]^2}{\rho(\vec{r})} d\vec{r}, \\ T_s^{\mathrm{NL}} &= \int W(\vec{r})\rho^{\alpha}(\vec{r}) k[\rho(\vec{r}),\rho(\vec{r}'), \\ &\quad \vec{r},\vec{r}']\rho^{\beta}(\vec{r}')W(\vec{r}') d\vec{r} d\vec{r}' + C, \end{aligned} \tag{32}$$

where C is introduced so that the KEDF can satisfy some limiting conditions discussed below. The validity of this weighted KEDF method within AMD-OFDDFT is guaranteed by E^{NL}, which corrects errors caused by approximate KEDFs inside the MT region. Since we now downscale the (inaccurate) KEDF contributions from the MT sphere region, the associated errors decrease and can be more accurately accounted for by E^{NL}. Consequently, determining the AMD energies in E^{NL} of Eq. (14) becomes easier because of the smaller magnitude of V_R^l, U_R^l, and K_R^l. Moreover, the weighted KEDF method can provide a more accurate description of the interstitial region because the effect of the rapidly varying electrons in the core region contributes less to the KEDF.

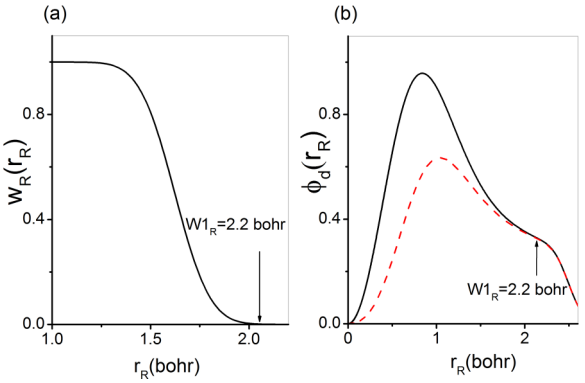

FIG. 2. (Color online) (a) Weighting function $w_R(r_R)$ inside the MT sphere with sphere radius $W1_R = 2.2$ bohr, generated with $w_R(W1_R) = 0.001$ and $w_R(r_{R,1}) = 0.75$ ($r_{R,1} = 1.4$ bohr) for the KEDF model in Eq. (32). (b) The original (solid line) and pseudized (dashed line) localized d radial basis function.

However, the behavior of the weighted KEDFs requires further consideration: in the uniform electron gas limit, the contribution from T_s^{NL} should be zero. To satisfy this limit, we add an extra term C to T_s^{NL} in Eq. (32), yielding

$$\int \rho_C^{\alpha} W(\vec{r}) k[\rho(\vec{r}),\rho(\vec{r}'),\vec{r},\vec{r}']W(\vec{r}')\rho_C^{\beta} d\vec{r} d\vec{r}' + C = 0, \tag{33}$$

where ρ_C is a constant density. However, for $\rho \neq$ const, the functional form of $C[\rho]$ is unknown. The above equation exists only in the uniform electron gas limit. For the present work, we approximate C as a constant. A future careful choice of the functional $C[\rho]$ might result in further improvements in material properties. Note that C arises from the use of T_s^{NL}. Thus, for local or semilocal KEDFs, there is no such concern about the term $C[\rho]$.

Because of the significant contribution of localized electrons to the total electron density, directly applying the weighted KEDFs to the whole density may still produce some errors, e.g., in the computation of the required average electron density ρ_0 for the response kernel in T_s^{NL} [23,24]. As an additional strategy for improving accuracy, we therefore introduce a pseudized wave function for the localized electron channel, similar to the density decomposition scheme used for the OFDFT treatment of Ag [39]. Inside the MT spheres, we scale the basis function $\phi_{R,l}$ to obtain a pseudized $\tilde{\phi}_{R,l}$:

$$\tilde{\phi}_{R,l}(r_R) = g_R(r_R)\phi_{R,l}(r_R), \tag{34}$$

where $\tilde{\phi}_l(r_R)$ is the pseudized smooth basis function, and $g_R(r_R)$ is a smoothing function. $g_R(r_R)$ can be chosen in many

different ways. Here, we simply choose

$$g_R(r_R) = \left\{1 + \mathrm{erf}\left[D_R\left(r_R + r_R^g\right)\right]\right\}/2. \quad (35)$$

The parameters D_R and r_R^g can be determined from function values at the sphere boundary $r_R = W1_R$ and the radial point having the maximum amplitude of the basis function $r_R = r_{\max}$:

$$g_R(W1_R) \lesssim 1, \quad g_R(r_{\max}) = \kappa,$$

where $g_R(W1_R)$ is slightly below one, to ensure that the smoothed wave function is quickly restored to its original values outside $W1_R$, so that the resulting error is negligible outside. The value κ determines the shape of the pseudized basis function inside the MT sphere. Its optimal value can be determined such that $\rho_0 \approx \langle\rho_I\rangle_I$, where $\langle\ldots\rangle_I$ denotes an average over the interstitial region. Note that smoothing is only required for the strongly localized d channel in transition metals, i.e., $g(r) = 1$ for the s and p channels in transition metals.

After the above pseudization of the localized electron basis function, we can write the smoothed total electron density as

$$\widetilde{\rho}_{\text{total}} = \sum_R \widetilde{\rho}_R + \rho_I, \quad (36)$$

where $\widetilde{\rho}_R = \sum_{lm,l'm'} N_{R,lm,l'm'} \widetilde{\psi}_{Rlm} \widetilde{\psi}_{Rl'm'}$ is the smoothed density inside the MT sphere. Obviously, $\rho = \tilde{\rho}$ in the interstitial region.

We thus use the rescaled $T^{\text{KEDF}}[\widetilde{\rho}]$ of Eq. (32) operating on a smooth electron density. By using pseudized localized basis functions, we can further reduce the unphysical interactions between delocalized and localized channels as discussed in Secs. I and II.

VI. SEARCHING FOR THE ANGULAR MOMENTUM DEPENDENT ENERGIES

We now introduce our method for finding a set of optimal AMD energies $\mathcal{P}_R = \{E_R^l, V_R^l, U_R^l, K_R^l\}$ for use in Eq. (14). As our current objective is an improved treatment of transition metals, here we only consider V_R^l, U_R^l, and K_R^l nonzero for the localized d channel, although generalization to other elements is straightforward. We aim to find these six optimal AMD energies, i.e., $E_R^{l=s,p,d}$, V_R^d, U_R^d, and K_R^d, by reproducing a small set of benchmark material properties determined by KSDFT-NLPS calculations using our AMD-OFDFT ansatz. We minimize the deviation

$$F[\mathcal{P}_R] = \sum_{i=1}^{N} C_i \left[\frac{X_i^{\text{OF}}[\mathcal{P}_R]}{X_i^{\text{KS}}} - 1\right]^2,$$

where $X_i^{\text{OF/KS}}$ denotes the ith property value derived from OFDFT and KSDFT, respectively. The benchmark properties may include occupation numbers of each l channel within the MT spheres, the equilibrium volume, the bulk modulus, and the energy differences between different structures. The parameter C_i weights the importance of property X_i. The feasibility of this optimization is ensured by the high numerical efficiency of OFDFT. In principle, the more properties included in F, the more transferable the energies $\mathcal{P}_R$ become. Conversely, a set of values $\mathcal{P}_R$ should be tested for transferability against properties not included in F. Thus we do not include properties of all structures but rather just fit to a minimal subset. We will demonstrate the transferability of the AMD energies in Sec. IX. Because U_R^d and K_R^d account for different physics than $E_R^{l=s,p,d}$ and V_R^d, our searching procedure is divided into two steps: we first search for a set of $\mathcal{P}_R^{EV} = \{E_R^l, V_R^d\}$ and then optimize $\mathcal{P}_R^{UK} = \{U_R^d, K_R^d\}$ for improved properties at the fixed $\mathcal{P}_R^{EV}$ found in the first step.

A good set of E_R^l and V_R^d must yield occupations comparable to KSDFT for each l channel and a total energy close to that from a KSDFT-NLPS calculation. This condition already proves quite stringent, strongly restricting useful values of E_R^l and V_R^d. The narrow range of these energies represents a challenge for applying global or local optimization methods, such as simulated annealing or simplex methods, without providing a good starting point. To find E_R^l and V_R^d, we thus adopt a simple adaptive-grid-based searching method that first considers only the occupation numbers: we calculate F on a uniform grid of E_R^p, E_R^d, and V_R^d values. For each grid point $[E_R^p, E_R^d, V_R^d]$, a change in E_R^s changes the occupation numbers of all the channels. The monotonic dependence of N_s on E_R^s (i.e., N_s will always increase for decreasing E_R^s) provides a way to quickly determine the bounds of E_R^s within which our OFDFT method gives satisfactory occupation numbers in comparison to KSDFT-NLPS calculations (see Fig. 3). For points within this E_R^s region, we then calculate the equilibrium volume and bulk modulus for a simple geometry, such as bulk fcc Ti. Only if these two properties compare well to KSDFT do we continue to calculate additional properties to fit against. We finally identify the $\mathcal{P}_R^{EV}$ with the smallest error F. We find that the AMD values determined with this algorithm already reproduce the KS benchmark surprisingly well (see Sec. IX). To further refine the values $\mathcal{P}_R^{EV}$, one may carry out a local optimization using, e.g., a simplex algorithm.

Nonzero values for U_R^d and K_R^d further improve the electron distribution within the localized d channel, yielding more accurate properties. In a second step, we search for $\mathcal{P}_R^{UK}$ on a uniform grid to further improve properties, such as the energy differences between a variety of bulk phases of titanium (see Sec. IX).

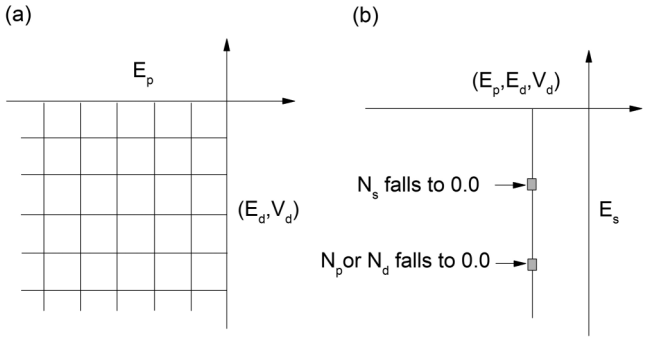

FIG. 3. Adaptive grid method for optimizing E_R^l and V_R^d. (a) Uniform grid for E_R^p, E_R^d, and V_R^d variables. (b) At a point $[E_R^p, E_R^d, V_R^d]$, we determine the upper and lower bounds for E_R^s using a coarse grid and then search for an appropriate E_R^s value on a finer grid between the bounds.

Once obtained for a given chemical element, the set of AMD energies, combined with the associated basis functions and scaling parameters for the KEDF, can be used for AMD-OFDFT simulation of materials containing that element, much like a pseudopotential. We envision a library of AMD energies and basis functions for the convenient use of AMD-OFDFT. Providing well-tested, transferable parametrizations for the most common elements is ongoing work, that will ultimately extend the applicability of OFDFT.

VII. FORCE FORMULA WITH PULAY CORRECTIONS

Given the force on the ions, we can optimize the ion positions to obtain an equilibrium geometry or we can carry out molecular dynamics simulations. For a general total energy functional $E_{\text{total}}[\rho,R]$, the force on an ion at position R is written as

$$F_R = -\frac{\partial E_{\text{total}}[\rho,R]}{\partial R} - \int \frac{\delta E_{\text{total}}[\rho,R]}{\delta\rho}\frac{d\rho}{dR}dr. \quad (37)$$

Here, the first and second terms are the Hellmann-Feynman and Pulay forces, respectively. The Pulay force arises from the atom-centered basis functions that explicitly depend on R. By adding the ion-ion interaction energy, the total energy functional becomes

$$E_{\text{total}}[\{N_R\},\rho_I,R] = T_s^{\text{KEDF}}[\rho] + E_{\text{H}}[\rho] + E_{\text{XC}}[\rho] + E_{\text{i-e}}^{\text{LPS}}[\rho,R] + E^{\text{NL}}[\{N_R\}] + E_{\text{i-i}}[R]. \quad (38)$$

Thus $\{N_R\}$, ρ_I, and R are three independent variables in E_{total}. The energy terms $E_{\text{i-e}}^{\text{LPS}}$ and $E_{\text{i-i}}$ explicitly contain the ion position R. Also, the applied KEDF model contains R explicitly because of the weighting function $W(\vec{r})$ of Eq. (30) introduced in Sec. V. Note that the nonlocal energy E^{NL} in Eq. (14) has no explicit dependence on R because the AMD energies, once obtained, are subsequently kept constant during the electronic structure optimization. Additionally, the N_R are independent variables in E_{total}. Thus, E^{NL} yields no contribution to the force. Consequently, the force formula in Eq. (37) is explicitly rewritten as

$$F_R = -\frac{dE_{\text{i-i}}}{dR} - \frac{\partial E_{\text{i-e,local}}}{\partial R} - \int \frac{\delta T_s^{\text{KEDF}}}{\delta W}\frac{dW}{dR}d\vec{r} - \int \left(V_{\text{KEDF}} + V_{\text{H}} + V_{\text{i-e}}^{\text{LPS}} + V_{\text{XC}}\right)\frac{d\rho_R}{dR}dr, \quad (39)$$

where we use the energy functional derivative in Eq. (B8) and $\frac{d\rho}{dR} = \frac{d\rho_R}{dR}$ since ρ_I is independent of R. According to Eq. (32), $\frac{\delta T_s^{\text{KEDF}}}{\delta W} = C_{\text{TF}}\rho^{5/3}(\vec{r}) + \frac{[\nabla\rho(\vec{r})]^2}{8\rho(\vec{r})} + \int \rho^{\alpha}(\vec{r})\,k[\rho(\vec{r}),\rho(\vec{r}'),\vec{r},\vec{r}']\,\rho^{\beta}(\vec{r}')\,W(\vec{r}')\,d\vec{r}' + \int \rho^{\beta}(\vec{r})\,k[\rho(\vec{r}),\rho(\vec{r}'),\vec{r},\vec{r}']\rho^{\alpha}(\vec{r}')W(\vec{r}')d\vec{r}'$.

As ρ_R is given by Eq. (2), the quantity $d\rho_R/dR$ can be expressed as

$$\frac{d\rho_R}{dR} = -\sum_{lm,l'm'} N_{R,lm,l'm'}\left[\psi^*_{R,lm}(\vec{r}_R)\frac{d\psi_{R,l'm'}(\vec{r}_R)}{d\vec{r}_R} + \psi_{R,l'm'}(\vec{r}_R)\frac{d\psi^*_{R,lm}(\vec{r}_R)}{d\vec{r}_R}\right], \quad (40)$$

by using $\frac{\partial\vec{r}_R}{\partial R} = -1$ since $\vec{r}_R = \vec{r} - R$. Although N_R is indexed with R, it does not explicitly depend on R as mentioned above.

VIII. A DOUBLE-SPHERE TECHNIQUE

To preserve the simplicity of OFDFT in practical implementations of the MT geometry, the basis functions inside the MT spheres are represented on a 3D uniform Cartesian grid by projecting from a radial mesh. From Sec. II we see that the basis functions are introduced inside the MT spheres but not in the interstitial region. Special care must be taken to properly treat the resulting discontinuity of the basis functions at the sphere boundary. Otherwise, this nonconforming grid problem (i.e., the mismatch between the sphere boundary and the Cartesian interstitial grid) will cause serious numerical instabilities for the convergence of the total energy with respect to grid size. In particular, small variations in geometry can produce artifacts, resulting in discontinuous energy curves. This problem becomes severe for basis functions with large amplitudes at the sphere boundary. In the following, we devise a double-sphere technique to solve this numerical problem. As shown in Fig. 4, we introduce inner and outer spheres with respective radii $W1_R$ and $W2_R$ centered on R: the basis functions are used within $W2_R$ and they are reduced between $W1_R$ and $W2_R$. In our double-sphere technique, the basis functions are modified as

$$\bar{\phi}_l(r_R) = \phi_l(r_R)f(r_R). \quad (41)$$

Here, the function $f(r_R)$ is introduced to smoothly decrease the amplitude of the basis function for $r_R > W1_R$. We choose the form

$$f^2(r) = \left\{1 - \text{erf}\left[A_R\left(r_R - r_R^f\right)\right]\right\}/2.0, \quad (42)$$

where the parameters A_R and r_R^f are determined by the function values $f(W1_R)$ and $f(W2_R)$. The $\bar{\phi}(r_R)$ are truncated outside the outer sphere. Both $f(W2_R)$ and $W2_R$ need to be chosen to reduce numerical noise (induced by the representation of the spheres on the uniform grid) below the accuracy requirement.

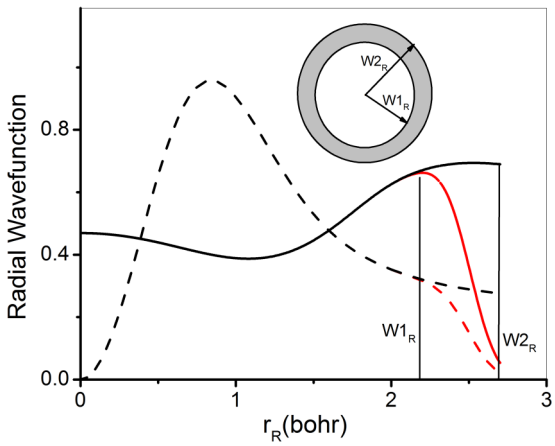

FIG. 4. (Color online) Double-sphere technique: the basis functions smoothly decrease in the region between $W1_R$ and $W2_R$, increasing numerical stability. Black curves: original basis functions ϕ_l; red curves: modified basis functions $\bar{\phi}_l$. Solid lines: s channel; dashed lines: d channel.

We set $f(W1_R) \lesssim 1$, so that the modified function $\bar{\phi}(r_R)$ is quickly restored to the original $\phi(r_R)$ for $r_R < W1_R$, such that the difference between $\bar{\phi}$ and ϕ_l is negligible within the inner sphere. In the geometry with atom-centered double spheres, the electron density inside the inner sphere is expressed only by $\bar{\phi}$, while the interstitial region starts at the inner-sphere boundary $W1_R$, and thus the electron density outside the inner spheres is given as a sum of the modulus squared of the reduced basis functions of Eq. (41) and ρ_I. We need to choose the sphere radii $W1_R$ and $W2_R$ so that no outer sphere overlaps with any other inner sphere. The introduction of the double spheres does not change the formalism and physics we discussed above, but significantly increases numerical stability.

An accurate evaluation of the potential matrix elements $\partial E/\partial N_R$ [see Eqs. (B3), (B4), and (B8)] by numerical integration within the double spheres can further increase numerical stability. The rapid spatial variations of the function $f^2(r)$ [(obtained from the product of the basis functions $\psi^*_{R,lm}\psi_{R,l'm'}$ in the expression of the density in Eq. (2)] require a fine grid to correctly capture the fast change in value between $W1_R$ and $W2_R$. However, we know the original basis functions ϕ_R and the energy potential $\delta E/\delta\rho$ are both slowly varying functions which can be accurately represented on a coarse grid. To reduce demands on grid discretization and maintain accuracy in the evaluation of $\partial E/\partial N_R$, we first project $f^2(r)$ from a radial grid onto a 3D uniform grid, which is two times denser than the coarse working grid on which we calculate the total energy and the corresponding potential. We then downsample $f^2(r)$ from the twice denser grid to the coarse working grid by a simple 3D interpolation [see Fig. 5(a)]. As shown in Appendix C and Fig. 5(b), the accuracy obtained can be similar to a calculation performed directly on the denser grid, while retaining the convergence

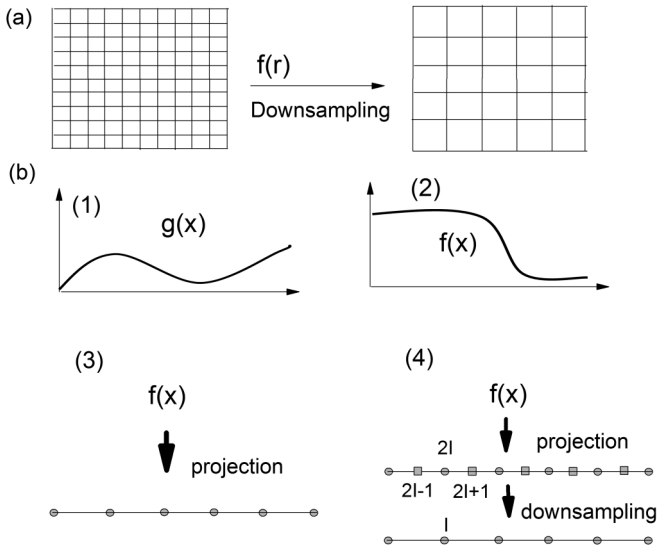

FIG. 5. Double-grid technique. (a) Downsampling the $f(r)$ from a two times denser grid to a coarse grid on which we calculate the total energy and potentials. (b) Example for integral $\int_A^B f(x)g(x)dx$: (1) smooth function $g(x)$; (2) fast changing $f(x)$; (3) projecting $f(x)$ onto a coarse grid directly; (4) projecting $f(x)$ onto a two times denser grid and then downsampling to the coarse grid.

speed of optimization on the coarser grid. It should be mentioned that the downsampling procedure is done only once before starting the total energy optimization. Consequently, the downsampling procedure increases numerical stability with negligible computational cost.

IX. COMPUTATIONAL DETAILS AND RESULTS

The entire AMD-OFDFT formalism outlined above has been implemented within PROFESS 2.0, a state-of-art OFDFT software package [51]. For implementation details for the Hartree, XC, LPS, and KEDF energies and the corresponding potentials, please refer to Ref. [52]. Here, we apply AMD-OFDFT to calculate various properties of the transition metal titanium and compare with other levels of approximation, to demonstrate the formalism and the associated numerical implementation.

In all our calculations, we use the Perdew-Burke-Ernzerhof (PBE) [53] form of the generalized gradient approximation as the exchange-correlation functional. Our KSDFT calculations are carried out using the ABINIT [46] software package. The Troullier-Martins (TM) form [54] of the NLPS with a nonlinear core correction [55] is used, as generated by the FHI98 code [56] with $r_{\text{cutoff}} = 2.2$ bohr for all l channels and $r_{\text{nlc}} = 1.2$ bohr as the cutoff radius for the core electron density. In KS-NLPS calculations, we use a plane-wave basis KE cutoff $E_{\text{cut}} = 1600$ eV (equivalent to 6400 eV in PROFESS 2.0) for the different Ti bulk phases, and the following Monkhorst-Pack grids [57] for k-point sampling: $30 \times 30 \times 20$ for hcp, $30 \times 30 \times 30$ for fcc and bcc, and $26 \times 26 \times 26$ for sc, within unit cells containing two, one, two, and one atoms, respectively.

The bulk-derived local pseudopotential (BLPS) [34] used in KS-BLPS and conventional OF-BLPS calculations is obtained by inverting the KS equations according to the procedure outlined in Ref. [35]. We use the Ti bcc phase for this inversion because we found that the hcp and fcc phases generate very scattered potential points. We also include the nonlinear core correction in the construction of the BLPS. The KS-BLPS calculations are done by ABINIT with the same plane-wave basis KE cutoff and k-point sampling as we use for the KS-NLPS calculations. Recall that OFDFT calculations do not require k-point sampling. For the conventional OF-BLPS calculation, we use a plane-wave basis KE cutoff of 6400 eV in PROFESS 2.0. For the AMD-OFDFT calculations, we use the s channel of the TM NLPS as the local pseudopotential; in this case, the plane-wave basis KE cutoff to converge the total energy with an error below 0.5 meV per titanium atom is 11 000 eV; although this cutoff sounds extreme, the calculations are very efficient, several orders of magnitude faster than KSDFT calculations. (We do not quote timings in this paper as the AMD-OFDFT code has not yet been optimized.) The basis functions inside the MT spheres are derived from a KS-NLPS calculation of the Ti fcc phase at its equilibrium lattice structure, using the method presented in Sec. III. We use $W1_R = 2.2$ bohr (same as r_{cutoff} of the NLPS) for the MT inner-sphere radius and $W2_R = 2.7$ bohr for the outer-sphere radius. $f^2(W1_R) = 0.995$ and $f^2(W2_R) = 0.1$ are used to solve for the parameters in Eq. (42) to achieve good numerical stability. Other choices of $0.1 \leqslant f^2(W2_R) \leqslant 0.3$ produce negligible changes in the total energy when using

TABLE I. Function values used to determine the scaling functions w_R and g_R, and resulting parameters.

w_R [see Eq. (31)]			
$w_R(W1_R)$	0.001	$w_R(W1_R - 0.8)$	0.75
B_R	3.35	r_R^w (bohr)	1.53
g_R [see Eq. (35)]			
$g_R(W1_R)$	0.995	$w_R(r_{\max})$	0.75
D_R	0.90	r_R^g (bohr)	0.31

the same AMD energies. A change in the shape of the basis functions between $W1_R$ and $W2_R$ only changes ρ_I during the total energy optimization but not the final total energy value. Values to determine the scaling functions w_R and g_R are listed in Table I. Changing these values is compensated by a change of the AMD energies in E^{NL}. Consequently, suitable parameter ranges are large: the choices of $w_R(W1_R - 0.8) \geqslant 0.55$ and $g_R(r_{\max}) \geqslant 0.45$ all give results very close to what we present here.

We use the search procedures presented in Sec. VI to determine the AMD energies $E_R^{l=s,p,d}$, V_R^d, U_R^d, and K_R^d by considering the following small set of properties of Ti described within KSDFT: the fcc occupation numbers N_l^{fcc} for each l channel, the fcc equilibrium volume V_0^{fcc}, the fcc bulk modulus B_0^{fcc}, the phase ordering energy $\Delta E_{\mathrm{fcc\text{-}hcp}}$ between fcc and hcp, and the absolute value of the fcc total energy. We denote use of only the first two terms of E^{NL} in Eq. (14) with AMD-OF1 while AMD-OF2 denotes use of all terms of E^{NL}. We obtained the following set of AMD energies after fitting: $E_R^s = -0.1133, E_R^p = 0.02, E_R^d = -0.38, V_R^d = 0.1, U_R^d = 0.252$, and $K_R^d = 0.5$ hartree. Using these parameters within AMD-OFDFT reproduces the KSDFT benchmark properties very well. We reported in Ref. [41] that calculations using this set of AMD energies deviate by 1% and 5% from the KS Ti fcc equilibrium volume and bulk modulus,

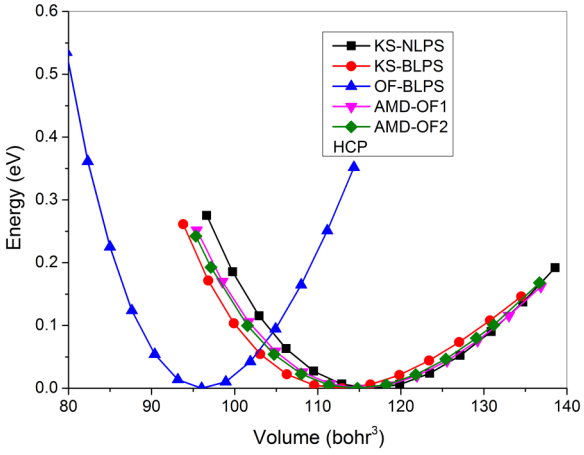

FIG. 6. (Color online) Energy versus volume for the Ti hcp phase, for five different theories (see text for details). Energy shifts of the total energy of the Ti hcp phase for the different levels of approximation are (in eV/atom) KS-NLPS: −268.410; KS-BLPS: −281.529; OF-BLPS: −279.672; AMD-OF1: −268.364; and AMD-OF2: −268.451.

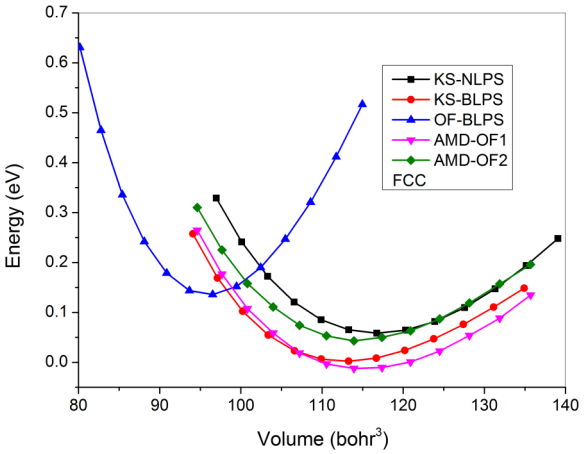

FIG. 7. (Color online) Energy versus volume for the Ti fcc phase, for five different theories.

respectively. Moreover, the phase ordering energy between fcc and hcp is quantitatively reproduced by AMD-OF2. We demonstrated good transferability of the AMD energies by applying them to bulk properties of Ti hcp, bcc, and sc phases, as well as the formation energies of a monovacancy in hcp Ti and of Ti hc(0001), fcc(100), and bcc(100) surfaces [41]. Here, we provide further tests of the model by investigating various types of mechanical deformations and comparing different levels of approximation. To further demonstrate the validity of the AMD-OFDFT formalism, the deformations applied here are much larger than normally used for calculating bulk properties (e.g., as presented in Ref. [41]).

Figures 6–9 show energy versus volume curves for Ti bulk hcp, fcc, bcc, and sc phases using different levels of DFT approximation. We shift the total energy of the ground-state hcp phase to zero for each theory, as shown in Fig. 6. It is clear that all methods produce smooth curves for all bulk phases investigated (as also shown in Figs. 10–13). This smoothness provides a strong test for the numerical stability of the AMD-OFDFT formalism. AMD-OFDFT substantially improves all results over the conventional OF-BLPS (see Figs. 6–9), e.g.,

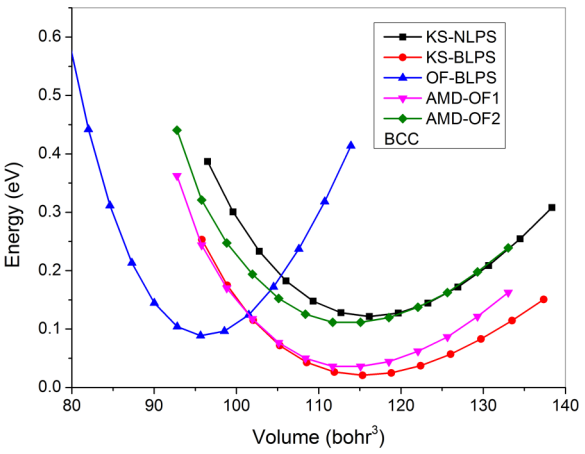

FIG. 8. (Color online) Energy versus volume for the Ti bcc phase, for five different theories.

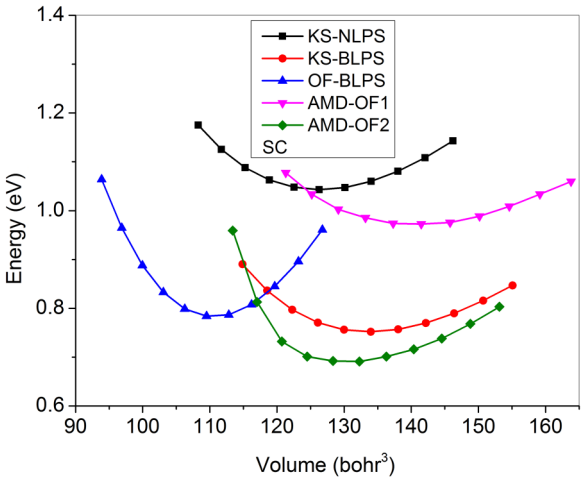

FIG. 9. (Color online) Energy versus volume for the Ti sc phase, for five different theories.

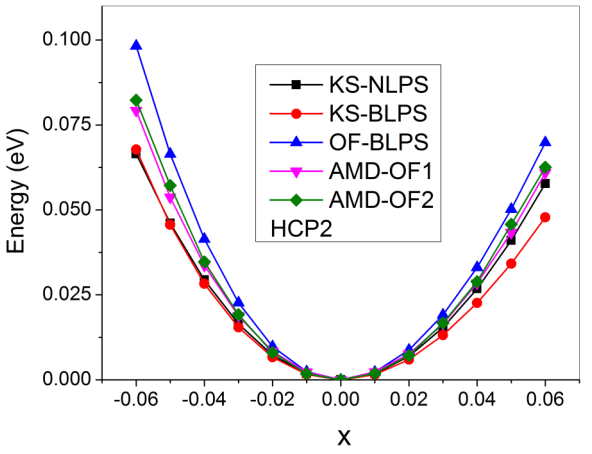

FIG. 11. (Color online) Energy versus strain x in hcp Ti. The applied strain mode is $(1+x,0,0;0,1-x,0;0,0,1)$.

the equilibrium volume and the energy response to system changes (see the curvature of the curves). In particular, conventional OFDFT volume predictions deviate about -20% from the KS-NLPS for all Ti phases, while our AMD-OF results produce equilibrium volumes only -1% smaller than KS benchmarks for hcp, fcc, and bcc phases and $+4\%$ for the sc phase. AMD-OFDFT produces a slowly changing energy curve in very good agreement with KS-NLPS, while OF-BLPS calculations exhibit much faster energy changes (i.e., too high bulk moduli) for all phases. For example, OF-BLPS predicts bulk moduli with about $+100\%$ error compared to AMD-OFDFT calculations that are very close to the benchmarks. In addition, conventional OFDFT, with its approximate KEDF and use of a BLPS, predicts a wrong phase ordering between fcc and bcc phases compared to KS-NLPS [41].

Although the KS-BLPS model, with its accurate KE, predicts accurate equilibrium volumes, energy versus volume curves, and qualitatively correct energy orderings between different phases, our numerically much faster AMD-OFDFT results are even closer to the KS-NLPS benchmarks. From the above comparison, we see that our AMD-OFDFT formalism provides an effective way to include the influence of an NLPS (hence the superior results compared to KS-BLPS) and to correct KE errors in KEDFs (hence the far superior results compared to OF-BLPS) in order to achieve an accurate description of system properties. The failure to describe the hypothetical sc Ti phase sufficiently well (see Fig. 9) is likely due to its much lower coordination number (six) compared to the other phases. The limit of transferability has been reached in this case and motivates future refinements to the model discussed earlier.

To understand the role of the AMD energies, we also compare the predictions of AMD-OF1 and AMD-OF2 in Figs. 6–9. It is evident that even with only the first two terms containing E_R^l and V_R^d in E^{NL}, AMD-OF1 reproduces very well the equilibrium volume and energy versus volume curves for Ti's hcp, fcc, and bcc phases compared to KS-NLPS benchmarks. However AMD-OF1 exhibits a $+10\%$ deviation from KS-NLPS for the equilibrium volume of sc Ti and a wrong phase ordering between Ti hcp and fcc phases, with a very small energy difference [41]. By including U_R^l and K_R^l in AMD-OF2 to correct the delocalization error in the KEDF

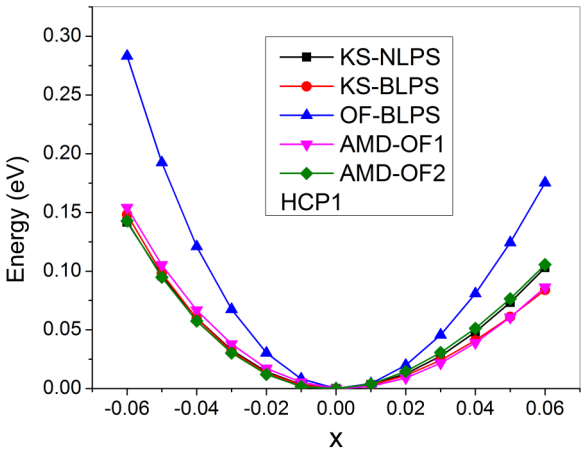

FIG. 10. (Color online) Energy versus strain x in hcp Ti. The applied strain mode is $(1+x,0,0;0,1+x,0;0,0,1)$.

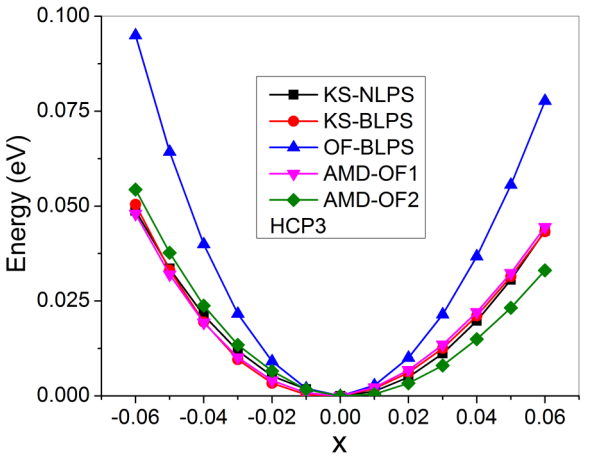

FIG. 12. (Color online) Energy versus strain x in hcp Ti. The applied strain mode is $(1,0,x;0,1,0;x,0,1)$.

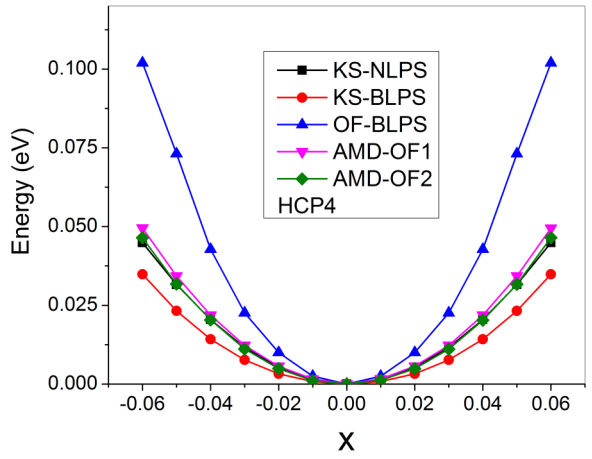

FIG. 13. (Color online) Energy versus strain x in hcp Ti. The applied strain mode is $[1,0,0;0,1,0;0,0,1+x]$.

(see Sec. II), we achieve the correct phase ordering (even the energy differences for fcc, bcc, and sc become comparable to KS-NLPS predictions), and an improved equilibrium volume for the Ti sc phase. Thus, corrections to the delocalization error are critical to reflect the effect of symmetry changes on properties.

Up to now, we have only examined the energy response to isotropic deformations of the bulk phases. To further evaluate the quality of the AMD-OFDFT formalism, we investigate other deformations of the ground-state hcp phase of Ti (see Figs. 10–13). We consider four independent deformation modes of the equilibrium hcp structure, with strain up to ±6%: Figs. 10 and 11 are for two independent deformations on the basal plane while keeping the other axis constant; Fig. 12 is for a pure shear deformation; Fig. 13 is for uniaxial deformations along the direction perpendicular to the basal plane. For details about the different types of deformations, see Ref. [19]. It is clear that our AMD-OFDFT approach agrees very well with KS-NLPS calculations, while conventional OFDFT significantly overestimates the energy increase with strain. The agreement seen here provides the foundation for AMD-OFDFT simulations of the mechanical properties of materials containing transition metals. AMD-OFDFT energy curves agree with KS-NLPS results for a wide range of deformations, providing a strong confirmation that the AMD-OFDFT formalism greatly improves the system density and the linear response function [3].

X. SUMMARY

We have shown that AMD-OFDFT substantially improves the accuracy of OFDFT for describing the transition metal Ti, and that the method exhibits quite good transferability. The accuracy and transferability of AMD-OFDFT is determined by the quality of E^{NL} (i.e., the AMD energies), the KEDF model, and the basis functions within the MT spheres. At present, we treat the AMD energies as constants for a given element and determine them by fitting to KS-NLPS benchmarks, neglecting their dependence on occupation numbers that may change as the system deforms. Nevertheless, we have demonstrated that the constant AMD energies feature good transferability. As we show in Sec. II, the good transferability is confirmed by a closer inspection of E^{NL}: the AMD energies depend only weakly on the small occupations of the delocalized channels (such as the s and p channels in transition metals), which are sensitive to system changes [41]. Although they do depend on the occupation of the localized channels (such as the d channel in transition metals), this occupation is not strongly influenced by system changes. Treating the AMD energies as constants is thus a good approximation. Future work considering the dependence of the AMD energies on the occupations may further enhance their transferability and accuracy. The generality of our AMD-OFDFT method also relies on the KEDF model. Modern two-point KEDFs [22–24] should be accurate enough to describe the interstitial region in different structures of at least any kind of metal and recent work has shown [26] that a density decomposition permits a modern KEDF (WGC99) [24] to also describe the interstitial regions in semiconductors. The accuracy of AMD-OFDFT is also related to the quality of the basis functions employed inside the MT spheres. For example, the AMD energies depend on the basis functions (see Appendix A), whose quality in turn determines how accurately the important ionic core region is represented. We derive ψ_R from KSDFT NLPS calculations of a suitable target system to explicitly consider the effect of the surrounding electronic structure. The ψ_R obtained in this way exhibit good transferability thus far, as we have shown above and in Ref. [41].

In conclusion, we have developed a general AMD-OFDFT method via a hybrid scheme based on a muffin tin geometry and have written the associated computer program for first-principles OFDFT simulations of materials that can now include transition metals. The AMD effects of the KE operator and of the interaction with the ionic cores are treated by using KSDFT-derived atom-centered basis functions inside the MT spheres, and by introducing an important nonlocal energy term to effectively correct the errors in the KEDF and the LPS. Our results for various properties of Ti show that including angular momentum dependence is essential for improving the electronic structure and the system response to external field changes, and thus system properties: AMD-OFDFT substantially improves the accuracy and general applicability of OFDFT. Our present results are all based on the WGC99 KEDF and approximations made to E^{NL}. More sophisticated KEDFs, or a more elaborate ansatz for E^{NL}, should further improve the accuracy and transferability of AMD-OFDFT.

ACKNOWLEDGMENTS

We gratefully acknowledge discussions with L.-W. Wang, L. Hung, C. Huang, and I. Shin. This work is supported by the Office of Naval Research (E.A.C.) and the SfB-041 ViCoM (F.L.). We thank Princeton University and the DOD supercomputing resource center for supercomputing time.

APPENDIX A: DERIVING $E^{\mathrm{NL}}[N_R]$

We provide further derivation of the parameters U_R^d and K_R^d in Eq. (14) by investigating their dependence on the occupation

numbers. From Ref. [41], we know

$$U_R^{\mathrm{KEDF},d} = 4\pi \int_{\mathrm{MT}} \frac{\delta^2 T_s^{\mathrm{KEDF}}}{\delta\rho^2}\bigg|_{\rho_R^0} \rho_{R,d}^2 r^2 dr. \quad \text{(A1)}$$

To obtain the dependence of $U_R^{\mathrm{KEDF},d}$ on N_R, one can perform a Taylor expansion for $U_R^{\mathrm{KEDF},d}$ around $N_{R,s/p}^0 = 0$ for transition metals. We consider here the TF and vW KEDFs because of their dominant contributions in the modern two-point KEDFs. For the TF KEDF, we apply the Taylor expansion to $\frac{\delta^2 \tilde{T}_s^{\mathrm{TF}}}{\delta\rho^2}|_{\rho_R^0}$ up to first order around $N_{R,s/p}^0 = 0$. We thus obtain

$$\begin{aligned} U_R^{\mathrm{TF},d} &= 4\pi \int_{\mathrm{MT}} \frac{\delta^2 \tilde{T}_s^{\mathrm{TF}}}{\delta\rho^2}\bigg|_{\rho_R^0} \rho_{R,d}^2 r^2 dr \\ &\approx 4\pi \int_{\mathrm{MT}} \Bigg[\left(N_{R,d}^{\mathrm{total}}\right)^{-\frac{1}{3}} \frac{\delta^2 \tilde{T}_s^{\mathrm{TF}}}{\delta\rho^2}\bigg|_{\rho_{R,d}} \\ &\quad + \sum_{l=s,p} \left(N_{R,d}^{\mathrm{total}}\right)^{-\frac{4}{3}} \frac{\delta^3 \tilde{T}_s^{\mathrm{TF}}}{\delta\rho^3}\bigg|_{\rho_{R,d}} N_{R,l}^{\mathrm{total}} \rho_{R,l} \Bigg] \rho_{R,d}^2 r^2 dr \\ &= N_{R,d}^{\mathrm{total},-\frac{1}{3}} B_{R,d}^{\mathrm{TF}} + \sum_{l=s,p} N_{R,d}^{\mathrm{total},-\frac{4}{3}} N_{R,l}^{\mathrm{total}} D_{R,d,l}^{\mathrm{TF}}. \end{aligned} \quad \text{(A2)}$$

The constants $B_{R,d}^{\mathrm{TF}} = 4\pi \int_{\mathrm{MT}} \frac{\delta^2 \tilde{T}_s^{\mathrm{TF}}}{\delta\rho^2}|_{\rho_{R,d}} \rho_{R,d}^2 r^2 dr$ and $D_{R,d,l}^{\mathrm{TF}} = 4\pi \int_{\mathrm{MT}} \frac{\delta^3 \tilde{T}_s^{\mathrm{TF}}}{\delta\rho^3}|_{\rho_{R,d}} \rho_{R,d}^2 \rho_{R,l} r^2 dr$ only depend on the fixed basis functions, and are thus system independent.

For the case of the vW KEDF, we also apply the Taylor expansion for $\frac{\delta^2 \tilde{T}_s^{\mathrm{vW}}}{\delta\rho^2}|_{\rho_R^0}$ up to first order around $N_{R,s/p}^0 = 0$:

$$\begin{aligned} U_R^{\mathrm{vW},d} &= 4\pi \int_{\mathrm{MT}} \frac{\delta^2 \tilde{T}_s^{\mathrm{vW}}}{\delta\rho^2}\bigg|_{\rho_R^0} \rho_{R,d}^2 r^2 dr \\ &= 4\pi \int_{\mathrm{MT}} \Bigg[\frac{1}{N_{R,d}^{\mathrm{total}}} \frac{\delta^2 \tilde{T}_s^{\mathrm{vW}}}{\delta\rho^2}\bigg|_{\rho_{R,d}} \\ &\quad + \sum_{l=s,p} \frac{N_{R,l}^{\mathrm{total}}}{\left(N_{R,d}^{\mathrm{total}}\right)^2} \frac{\delta^3 \tilde{T}_s^{\mathrm{vW}}}{\delta\rho^3}\bigg|_{\rho_{R,d}} \rho_{R,l} \Bigg] \rho_{R,d}^2 r^2 dr \\ &= \frac{1}{N_{R,d}^{\mathrm{total}}} B_{R,d}^{\mathrm{vW}} + \sum_{l=s,p} \frac{1}{\left(N_{R,d}^{\mathrm{total}}\right)^2} N_{R,l}^{\mathrm{total}} D_{R,d,l}^{\mathrm{vW}}. \end{aligned} \quad \text{(A3)}$$

The constants $B_{R,d}^{\mathrm{vW}} = 4\pi \int_{\mathrm{MT}} \frac{\delta^2 \tilde{T}_s^{\mathrm{vW}}}{\delta\rho^2}|_{\rho_{R,d}} \rho_{R,d}^2 r^2 dr$ and $D_{R,d,l}^{\mathrm{vW}} = 4\pi \int_{\mathrm{MT}} \frac{\delta^3 \tilde{T}_s^{\mathrm{vW}}}{\delta\rho^3}|_{\rho_{R,d}} \rho_{R,l} \rho_{R,d}^2 r^2 dr$ are only dependent on the fixed basis functions, and are thus system independent again. Thus, we see $U_R^{\mathrm{KEDF},d}$ can be approximated as

$$\begin{aligned} U_R^{\mathrm{TF+vW},d} &\approx \left(N_{R,d}^{\mathrm{total}}\right)^{-\frac{1}{3}} B_{R,d}^{\mathrm{TF}} + \sum_{l=s,p} \left(N_{R,d}^{\mathrm{total}}\right)^{-\frac{4}{3}} N_{R,l}^{\mathrm{total}} D_{R,d,l}^{\mathrm{TF}} \\ &\quad + \left(N_{R,d}^{\mathrm{total}}\right)^{-1} B_{R,d}^{\mathrm{vW}} + \sum_{l=s,p} \left(N_{R,d}^{\mathrm{total}}\right)^{-2} N_{R,l}^{\mathrm{total}} D_{R,d,l}^{\mathrm{vW}} \\ &\approx \left(N_{R,d}^{\mathrm{total}}\right)^{-\frac{1}{3}} B_{R,d}^{\mathrm{TF}} + \left(N_{R,d}^{\mathrm{total}}\right)^{-1} B_{R,d}^{\mathrm{vW}} \\ &\quad + \sum_{l=s,p} \tilde{D}_{R,d,l}^{\mathrm{TF+vW}} N_{R,l}^{\mathrm{total}}. \end{aligned} \quad \text{(A4)}$$

For the parameter $K_R^{\mathrm{KEDF},d}$, we have [41]

$$K_R^{\mathrm{KEDF},d} = 4\pi \int_{\mathrm{MT}} \frac{\delta^3 \tilde{T}_s^{\mathrm{KEDF}}}{\delta\rho^3}\bigg|_{\rho_R^0} \rho_{R,d}^3 r^2 dr. \quad \text{(A5)}$$

For the case of TF KEDF, a Taylor expansion around $N_{R,s/p}^0 = 0$ yields

$$\begin{aligned} K_R^{\mathrm{TF},d} &= 4\pi \int_{\mathrm{MT}} \frac{\delta^3 \tilde{T}_s^{\mathrm{TF}}}{\delta\rho^3}\bigg|_{\rho_R^0} \rho_{R,d}^3 r^2 dr \\ &= 4\pi \int_{\mathrm{MT}} \Bigg[\left(N_{R,d}^{\mathrm{total}}\right)^{-\frac{4}{3}} \frac{\delta^3 \tilde{T}_s^{\mathrm{TF}}}{\delta\rho^3}\bigg|_{\rho_{R,d}} \\ &\quad + \sum_{l=s,p} \left(N_{R,d}^{\mathrm{total}}\right)^{-\frac{7}{3}} N_{R,l}^{\mathrm{total}} \frac{\delta^4 \tilde{T}_s^{\mathrm{TF}}}{\delta\rho^4}\bigg|_{\rho_{R,d}} \rho_{R,l} \Bigg] \rho_{R,d}^3 r^2 dr \\ &= \left(N_{R,d}^{\mathrm{total}}\right)^{-\frac{4}{3}} G_{R,d}^{\mathrm{TF}} + \left(N_{R,d}^{\mathrm{total}}\right)^{-\frac{7}{3}} N_{R,l}^{\mathrm{total}} H_{R,d,l}^{\mathrm{TF}}, \end{aligned} \quad \text{(A6)}$$

where $G_{R,d}^{\mathrm{TF}} = 4\pi \int_{\mathrm{MT}} \frac{\delta^3 \tilde{T}_s^{\mathrm{TF}}}{\delta\rho^3}|_{\rho_{R,d}} \rho_{R,d}^3 r^2 dr$ and $H_{R,d,l}^{\mathrm{TF}} = 4\pi \int_{\mathrm{MT}} \frac{\delta^4 \tilde{T}_s^{\mathrm{TF}}}{\delta\rho^4}|_{\rho_{R,d}} \rho_{R,l} \rho_{R,d}^3 r^2 dr$ are dependent on the radial basis functions inside the MT spheres.

For the case of the vW KEDF, again, using a Taylor expansion around $N_{R,s/p}^0 = 0$, we find

$$\begin{aligned} K_R^{\mathrm{vW},d} &= 4\pi \int_{\mathrm{MT}} \frac{\delta^3 \tilde{T}_s^{\mathrm{vW}}}{\delta\rho^3}\bigg|_{\rho_R^0} \rho_{R,d}^3 r^2 dr \\ &= 4\pi \int_{\mathrm{MT}} \Bigg[\frac{1}{\left(N_{R,d}^{\mathrm{total}}\right)^2} \frac{\delta^3 \tilde{T}_s^{\mathrm{vW}}}{\delta\rho^3}\bigg|_{\rho_{R,d}} \\ &\quad + \frac{1}{\left(N_{R,d}^{\mathrm{total}}\right)^3} \frac{\delta^4 T_s^{\mathrm{vW}}}{\delta\rho^4}\bigg|_{\rho_{R,d}} N_{R,l}^{\mathrm{total}} \rho_{R,l} \Bigg] \rho_{R,d}^3 r^2 dr \\ &= \frac{1}{\left(N_{R,d}^{\mathrm{total}}\right)^2} G_{R,d}^{\mathrm{vW}} + \frac{1}{\left(N_{R,d}^{\mathrm{total}}\right)^3} N_{R,l}^{\mathrm{total}} H_{R,d,l}^{\mathrm{vW}}, \end{aligned} \quad \text{(A7)}$$

where $G_{R,d}^{\mathrm{vW}} = 4\pi \int_{\mathrm{MT}} \frac{\delta^3 \tilde{T}_s^{\mathrm{vW}}}{\delta\rho^3}|_{\rho_{R,d}} \rho_{R,d}^3 r^2 dr$ and $H_{R,d,l}^{\mathrm{vW}} = 4\pi \int_{\mathrm{MT}} \frac{\delta^4 \tilde{T}_s^{\mathrm{vW}}}{\delta\rho^4}|_{\rho_{R,d}} \rho_{R,l} \rho_{R,d}^3 r^2 dr$ are only given by the radial basis functions inside the MT spheres. Therefore, we have

$$\begin{aligned} K_R^{\mathrm{TF+vW},d} &\approx \left(N_{R,d}^{\mathrm{total}}\right)^{-\frac{4}{3}} \left(G_{R,d}^{\mathrm{TF}} - \sum_{l=s,p} \frac{N_{R,l}^{\mathrm{total}}}{N_{R,d}^{\mathrm{total}}} H_{R,d,l}^{\mathrm{TF}} \right) \\ &\quad + \left(N_{R,d}^{\mathrm{total}}\right)^{-2} G_{R,d}^{\mathrm{vW}} + \sum_{l=s,p} \left(N_{R,d}^{\mathrm{total}}\right)^{-3} N_{R,l}^{\mathrm{total}} H_{R,d,l}^{\mathrm{vW}} \\ &\approx \left(N_{R,d}^{\mathrm{total}}\right)^{-\frac{4}{3}} G_{R,d}^{\mathrm{TF}} + \left(N_{R,d}^{\mathrm{total}}\right)^{-2} G_{R,d}^{\mathrm{vW}} \\ &\quad + \sum_{l=s,p} \tilde{H}_{R,d,l}^{\mathrm{TF+vW}} N_{R,l}^{\mathrm{total}}. \end{aligned} \quad \text{(A8)}$$

APPENDIX B: DETAILS OF THE TOTAL ENERGY MINIMIZATION

In each optimization step, for a given $Y = \{M_R\}, Q_I$, we need to compute $L[Y]$ and the corresponding gradient dL/dY

to calculate the line search direction for updating Y. We calculate dE/dY by applying the chain rule to the energy terms including $T_s^{\mathrm{KEDF}}[\rho]$, $E_{\mathrm{XC}}[\rho]$, $E_{\mathrm{H}}[\rho]$, and $E_{\mathrm{i\text{-}e}}^{\mathrm{LPS}}[\rho]$ in Eq. (4) as

$$\frac{\partial E}{\partial M_R} = \frac{\partial E}{\partial N_R}\frac{dN_R}{dM_R}; \tag{B1}$$

$$\frac{\partial E}{\partial Q_I} = \frac{\delta E[\rho]}{\delta \rho}\frac{\partial \rho}{\partial \rho_I}\frac{d\rho_I}{dQ_I}. \tag{B2}$$

Here,

$$\frac{\partial E}{\partial N_R} = \int_{\mathrm{MT}} \frac{\delta E[\rho]}{\delta \rho}\frac{\partial \rho}{\partial N_R} d\vec{r}; \tag{B3}$$

$$\frac{\partial \rho}{\partial N_{R,lm,l'm'}} = \psi^*_{R,lm}\psi_{R,l'm'}; \tag{B4}$$

$$\frac{dN_R}{dM_R} = 6M_R(1-M_R); \tag{B5}$$

$$\frac{\partial \rho}{\partial \rho_I} = 1; \tag{B6}$$

$$\frac{d\rho_I}{dQ_I} = 6Q_I(1-Q_I)/dV; \tag{B7}$$

$$\frac{\delta E[\rho]}{\delta \rho} = V_{\mathrm{KEDF}} + V_{\mathrm{H}} + V_{\mathrm{XC}} + V_{\mathrm{i\text{-}e}}^{\mathrm{LPS}}, \tag{B8}$$

where V_{KE}, V_{H}, V_{XC}, and $V_{\mathrm{i\text{-}e}}^{\mathrm{LPS}}$ are the KE potential, Hartree potential, exchange-correlation energy potential, and local pseudopotential, respectively. $\frac{dN_{\mathrm{total}}}{dY} = \frac{dN_{\mathrm{total}}}{dX}\frac{dX}{dY}$ and $\frac{dE^{\mathrm{NL}}}{dY} = \frac{dE^{\mathrm{NL}}}{dX}\frac{dX}{dY}$, where $X = \{N_R\},\rho_I$, can be calculated by using Eqs. (B5) and (B7). During the total energy minimization, we update the chemical potential in Eq. (27) in each iteration by

$$\mu = \frac{\left\langle \frac{dE}{dY} \middle| Y \right\rangle}{\left\langle \frac{dN_{\mathrm{total}}}{dY} \middle| Y \right\rangle}. \tag{B9}$$

In each minimization step, we note the total electron number is not strictly conserved after the line search. Therefore, we renormalize the total number of electrons

$$Y = Y_0 - (N_{\mathrm{total}}[Y_0] - N_0)\frac{\frac{dN_{\mathrm{total}}}{dY}}{\left\langle \frac{dN_{\mathrm{total}}}{dY} \middle| \frac{dN_{\mathrm{total}}}{dY} \right\rangle},$$

where Y_0 is the variable obtained directly by the line search and the corrected Y serves as the initial variable for the next optimization iteration. This correction step does not change the decrease of the total energy obtained in the line search procedure. As the optimization converges, this correction becomes smaller and smaller.

APPENDIX C: DOWNSAMPLING TECHNIQUE

We illustrate the principle using a one-dimensional function as an example. We want to accurately calculate the integral $\int_A^B f(x)g(x)dx$ on a coarse grid, where $f(x)$ is a rapidly fluctuating function while $g(x)$ varies slowly over all space [see Fig. 5(b)]. We apply the relationship

$$\tilde{f}(x_I) = 0.5 * \left[f(x_{2I}) + \frac{f(x_{2I-1}) + f(x_{2I+1})}{2} \right] \tag{C1}$$

between the function on the dense $(2I)$ and coarse (I) grids. The numerical integration on the coarse grid can then be written as

$$\begin{aligned}
\int_A^B f(x)g(x)dx &\approx \Delta x \sum_I g(x_I) * \tilde{f}(x_I) = \Delta\hat{x} \sum_I \left[f(\hat{x}_{2I}) + \frac{f(\hat{x}_{2I-1}) + f(\hat{x}_{2I+1})}{2} \right] * g(x_I) \\
&= \Delta\hat{x} \sum_I \left[f(\hat{x}_{2I}) + \frac{f(\hat{x}_{2I-1}) + f(\hat{x}_{2I+1})}{2} \right] * g(\hat{x}_{2I}) \\
&= \Delta\hat{x} \sum_I f(\hat{x}_{2I})g(\hat{x}_{2I}) + f(\hat{x}_{2I-1})\frac{g(\hat{x}_{2I-2}) + g(\hat{x}_{2I})}{2} + f(\hat{x}_{2I+1})\frac{g(\hat{x}_{2I}) + g(\hat{x}_{2I+2})}{2} \\
&= \Delta\hat{x} \sum_I [f(\hat{x}_{2I-1})\bar{g}(\hat{x}_{2I-1}) + f(\hat{x}_{2I})\bar{g}(\hat{x}_{2I}) + f(\hat{x}_{2I+1})\bar{g}(\hat{x}_{2I+1})],
\end{aligned} \tag{C2}$$

where $\hat{x}_{2I} = x_I$ and $\Delta\hat{x} = 0.5\Delta x$. Since $g(x)$ only varies slowly, $\bar{g}(x)$ can be given in good accuracy by a simple interpolation. From the above derivation, we can obtain the high accuracy of the integral performed on a coarse grid, comparable to the direct integration on the two times denser grid. This provides an efficient way for us to obtain accurate potential matrix elements $\frac{dE}{dN}$ inside the MT spheres with a reasonable grid size.

[1] P. Hohenberg and W. Kohn, Phys. Rev. **136**, B864 (1964).
[2] W. Kohn and L. J. Sham, Phys. Rev. **140**, A1133 (1965).
[3] Y. A. Wang and E. A. Carter, in *Theoretical Methods in Condensed Phase Chemistry*, edited by S. D. Schwartz (Kluwer, Dordrecht, 2000), p. 117.
[4] E. A. Carter, Science **321**, 800 (2008).
[5] D. R. Bowler and T. Miyazaki, Rep. Prog. Phys. **75**, 036503 (2012).
[6] S. Goedecker. Rev. Mod. Phys. **71**, 1085 (1999).
[7] W. Lu and C. M. Lieber, Nat. Mater. **6**, 841 (2007).
[8] X. Li, Y. Wei, L. Lu, K. Lu, and H. Gao, Nature (London) **464**, 877 (2010).

[9] T. C. Hufnagel, Nat. Mater. **3**, 666 (2004).
[10] L. Hung and E. A. Carter, Chem. Phys. Lett. **475**, 163 (2009).
[11] L. Hung and E. A. Carter, J. Phys. Chem. C **115**, 6269 (2011).
[12] D. J. González, L. E. González, and M. J. Stott, Phys. Rev. Lett. **92**, 085501 (2004).
[13] M. Chen, L. Hung, C. Huang, J. Xia, and E. A. Carter, Mol. Phys. (to be published).
[14] J. A. Anta and P. A. Madden, J. Phys.: Condens. Matter **11**, 6099 (1999).
[15] S. C. Watson and P. A. Madden, PhysChemComm **1**, 1 (1998).
[16] L. Hung and E. A. Carter, Modell. Simul. Mater. Sci. Eng. **19**, 045002 (2011).
[17] Q. Peng, X. Zhang, C. Huang, E. A. Carter, and G. Lu, Modell. Simul. Mater. Sci. Eng. **18**, 075003 (2010).
[18] I. Shin, A. Ramasubramaniam, C. Huang, L. Hung, and E. A. Carter, Philos. Mag. **89**, 3195 (2009).
[19] I. Shin and E. A. Carter, Modell. Simul. Mater. Sci. Eng. **20**, 015006 (2012).
[20] L. H. Thomas, Proc. Cambridge Philos. Soc. **23**, 542 (1927); E. Fermi, Rend. Acad. Naz. Lincei **6**, 602 (1927); Z. Phys. **48**, 73 (1928).
[21] C. F. v. Weizsäcker, Z. Phys. **96**, 431 (1935).
[22] E. Chacón, J. E. Alvarellos, and P. Tarazona, Phys. Rev. B **32**, 7868 (1985).
[23] L.-W. Wang and M. P. Teter, Phys. Rev. B **45**, 13196 (1992).
[24] Y. A. Wang, N. Govind, and E. A. Carter, Phys. Rev. B **60**, 16350 (1999).
[25] C. Huang and E. A. Carter, Phys. Rev. B **81**, 045206 (2010).
[26] J. Xia and E. A. Carter, Phys. Rev. B **86**, 235109 (2012).
[27] M. Foley and P. A. Madden, Phys. Rev. B **53**, 10589 (1996).
[28] B. J. Jesson, M. Foley, and P. A. Madden, Phys. Rev. B **55**, 4941 (1997).
[29] D. Garca-Aldea and J. E. Alvarellos, J. Chem. Phys. **127**, 144109 (2007).
[30] J. P. Perdew and L. A. Constantin, Phys. Rev. B **75**, 155109 (2007).
[31] V. V. Karasiev, R. S. Jones, S. B. Trickey, and F. E. Harris, Phys. Rev. B **80**, 245120 (2009).
[32] V. V. Karasiev, D. Chakraborty, O. A. Shukruto, and S. B. Trickey, Phys. Rev. B **88**, 161108(R) (2013).
[33] S. Watson, B. J. Jesson, E. A. Carter, and P. A. Madden, Europhys. Lett. **41**, 37 (1998).
[34] B. Zhou, Y. A. Wang, and E. A. Carter, Phys. Rev. B **69**, 125109 (2004).
[35] C. Huang and E. A. Carter, Phys. Chem. Chem. Phys. **10**, 7109 (2008).
[36] D. J. González, L. E. González, J. M. López, and M. J. Stott, Phys. Rev. B **65**, 184201 (2002).
[37] V. V. Karasiev, T. Sjostrom, and S. B. Trickey, Phys. Rev. E **86**, 056704 (2012).
[38] V. V. Karasiev and S. B. Trickey, Comput. Phys. Commun. **183**, 2519 (2012).
[39] C. Huang and E. A. Carter, Phys. Rev. B **85**, 045126 (2012).
[40] B. Zhou and E. A. Carter, J. Chem. Phys. **122**, 184108 (2005).
[41] Y. Ke, F. Libisch, J. Xia, L.-W. Wang, and E. A. Carter, Phys. Rev. Lett. **111**, 066402 (2013).
[42] D. Singh, *Plane Waves, Pseudopotentials and the LAPW Method* (Kluwer Academic, Dordrecht, 1994); K. Schwarz, P. Blaha, and G. K. H. Madsen, Comput. Phys. Commun. **147**, 71 (2002).
[43] O. K. Andersen, Phys. Rev. B **12**, 3060 (1975); M. Methfessel, *ibid*. **38**, 1537 (1988).
[44] V. I. Lebedev, Zh. Vychisl. Mat. Mat. Fiz. **16**, 293 (1976).
[45] V. I. Anisimov, J. Zaanen, and O. K. Andersen, Phys. Rev. B **44**, 943 (1991).
[46] X. Gonze *et al*., Comput. Phys. Commun. **180**, 2582 (2009); X. Gonze *et al*., Z. Kristallogr. **220**, 558 (2005).
[47] H. William, B. P. Flannery, S. A. Teukolsky, and W. T. Vetterling, *Numerical Recipes: The Art of Scientific Computing*, 3rd ed. (Cambridge University Press, Cambridge, 2007), Sec. 17.1.
[48] X. P. Li, R. W. Nunes, and D. Vanderbilt, Phys. Rev. B **47**, 10891 (1993).
[49] M. R. Hestenes and E. Stiefel, J. Res. Natl. Bur. Stand. **49**, 409 (1952).
[50] J. Nocedal, Math. Comput. **35**, 773 (1980).
[51] L. Hung, C. Huang, I. Shin, G. S. Ho, V. L. Lignères, and E. A. Carter, Comput. Phys. Commun. **181**, 2208 (2010).
[52] G. S. Ho, V. L. Lignères, and E. A. Carter, Comput. Phys. Commun. **179**, 839 (2008).
[53] J. P. Perdew, K. Burke, and M. Ernzerhof, Phys. Rev. Lett. **77**, 3865 (1996).
[54] N. Troullier and J. L. Martins, Phys. Rev. B **43**, 1993 (1991).
[55] S. G. Louie, S. Froyen, and M. L. Cohen, Phys. Rev. B **26**, 1738 (1982).
[56] M. Fuchs and M. Scheffler, Comput. Phys. Commun. **119**, 67 (1999).
[57] H. J. Monkhorst and J. D. Pack, Phys. Rev. B **13**, 5188 (1976).